Intercritical annealing of cold-rolled ferrite-pearlite steel: Microstructure evolutions and phase transformation kinetics

Julien Teixeira, Marc Moreno, S.Y. P. Allain, C. Oberbillig, G. Geandier, F. Bonnet

Intercritical annealing of cold-rolled ferrite-pearlite steel: microstructure evolutions and phase transformation kinetics

J. Teixeira[a,b*], M. Moreno[a,b], S.Y.P. Allain[a,b], C. Oberbillig[c], G. Geandier[a,b], F. Bonnet[c]

[a]Institut Jean Lamour, UMR 7198 CNRS – Univ. Lorraine, Nancy, France.
[b]Laboratory of Excellence "Design of Alloy Metals for Low-mass Structures" (DAMAS), Univ. Lorraine.
[c]ArcelorMittal Maizières Research SA, Automotive Products Research Center, Maizières les Metz, France.

Abstract
The manufacturing of Dual-Phase steels includes as a crucial step the annealing of a cold-rolled ferrite-pearlite (F/P) microstructure, which involves numerous and interacting metallurgical mechanisms, namely recovery/recrystallization of ferrite, globularization, manganese enrichment, coarsening of cementite and finally austenite transformation. Present study focuses on the austenite transformation considering its interaction with the ferrite recrystallization and the influence of the chemical composition of the cementite. The behavior of a cold-rolled F/P microstructure is studied at three heating rates to induce weak and strong interactions between the mechanisms, in particular using post mortem microstructure observations but also in situ High Energy X-Ray Diffraction experiments on a synchrotron beamline.
Slow heating leads to a necklace austenite distribution whereas fast heating conducts to a banded topology. This particular microstructure morphogenesis is explained by the presence of numerous intergranular (or isolated) carbides inside the ferrite matrix, inherited from the hot-rolling. Thermokinetic analysis accounting for the cementite composition shows that the pearlite islands transformation necessarily involves the partition of substitutional elements. Conversely, the dissolving isolated carbides undergo a partition/partitionless transition on heating. After the dissolution of the cementite, a final ferrite/austenite transformation takes place. The phase transformation kinetics increases with increasing heating rates, despite the thermal-activated nature of the austenite growth process. This is interpreted thanks to kinetic simulations with DICTRA software, which allow to analyze the austenite growth regimes involving or not the partition of the alloying elements.

Keywords
Austenite transformation, Dual-Phase steels, intercritical annealing, HEXRD, Cementite dissolution, DICTRA simulations

*Corresponding author
Julien Teixeira
Institut Jean Lamour
CNRS – Université de Lorraine
Campus Artem
2, allée André Guinier
BP 50840
F-54011 NANCY CEDEX
FRANCE
tel +33 3 72 74 26 90
fax +33 3 72 74 24 01
julien.teixeira@univ-lorraine.fr

Author's email addresses:
Marc Moreno: m_moreno@hotmail.fr
S.Y.P. Allain: sebastien.allain@univ-lorraine.fr
C. Oberbillig: carla.oberbillig@arcelormittal.com
G. Geandier: guillaume.geandier@univ-lorraine.fr
F. Bonnet : frederic.bonnet@arcelormittal.com

1 Introduction

Dual-Phase (DP) steels are largely employed in the automotive industry for their excellent strength / ductility trade-off and their weight reduction potential [1–7]. DP steels have a composite microstructure composed of carbon-rich martensite islands embedded in a matrix of softer ferrite [1] and occasionally containing bainite [8]. The tensile properties (yield strength, ultimate tensile strength, uniform elongation) depend strongly on the volume fraction of the martensite [9–11]. Its three-dimensional features, i.e. the spatial and morphological distribution of the phases, also influence the fracture properties and the resistance to damage. For example, banded structures of elongated martensite islands aligned in the rolling direction have a negative impact on the damage properties and on the local ductility [12−15]. Conversely, the tensile properties depend weakly on the spatial organization of the phases [12].

Precise control of the properties requires thus to understand how the microstructures are formed during the thermomechanical processing of DP steels. The sequence of treatments starts with a hot-rolling operation in the full-austenite domain. After a cooling sequence during the coiling operation, a cold-rolling step at room temperature is applied in addition to obtain thinner products of interest for automotive construction. The crucial step is the final intercritical annealing [16–18]: a partial austenite transformation takes place in the biphasic ferrite+austenite domain of stability; during the final cooling, the austenite transforms progressively again to ferrite at high temperature, then in bainite and finally into martensite. Hence, the final martensite microstructure (previously austenite) is largely inherited from the intercritical annealing. Many investigations considered the austenite transformation occurring during this step, focusing on two main features: the austenite morphogenesis and the phase transformation kinetics.

Important parameter of the intercritical annealing is the heating rate up to the soaking temperature. Slow heating leads to a necklace morphology of the austenite, whereas fast heating leads to a banded morphology, with strong impact on the mechanical behavior [19–21]. This morphological transition is mostly specific to cold-rolled ferrite-pearlite initial microstructures [2,22–27]. Except in [16,27,28], it does not occur for other initial microstructures such as hot-rolled ferrite-pearlite [23,25] or mixtures including bainite and/or martensite [2]. Faster heating leads to faster austenite transformation kinetics [2,22–25,28], despite the thermal-activated nature of the nucleation-growth process and whatever the initial microstructure. After fast heating, the final fraction of austenite can overcome the value expected from thermodynamics [24,29]. The local chemical compositions in the final microstructure may remain out of equilibrium. The transformation kinetics can follow different stages involving or not the partition of the alloying elements [1,30,31].

These complex evolutions come from the interactions of the austenite transformation with other metallurgical processes. In the case of an initial cold-rolled ferrite-pearlite microstructure, the cementite and the ferrite matrix undergo several phenomena during the heating and before the start of the austenite transformation [32,33]. The cementite carbides undergo fragmentation, spheroidization and coarsening; these processes are accelerated by the defects introduced by the cold-rolling [34–40]. This modifies the size and the spatial distribution of the carbides and thus of the initial nucleation sites and the carbon sources for the austenite. The chemical composition of the carbides also evolves during heating; enrichment in Mn and Cr stabilizes the carbides, slows-down their dissolution and hence the austenite transformation [41–48]. Actually, the initial composition of the carbides before the annealing treatment already depends on the metallurgical history of the hot band (so-called inheritance effects) [49].

As for the ferrite matrix, it becomes highly defected after the cold-rolling. It undergoes on heating recovery and then recrystallization processes [50–52]. During slow heating, the ferrite recrystallization is complete before the start of the austenite transformation, which takes place, except for the pearlitic ferrite, inside a fully recrystallized microstructure. ("Weak" interaction between austenite transformation and ferrite recrystallization as the mechanisms occur sequentially). In the case of slow heating, there is a general agreement in literature regarding the austenite morphogenesis. The necklace morphology comes from the nucleation and growth of the austenite at the boundaries of the large and equiaxed ferrite grains. Point of disagreement concerns the nature of the nucleation sites: either intergranular carbide, or "empty" ferrite grain boundaries. During fast heating, the austenite transformation and the ferrite recrystallization take place simultaneously (strong interaction). The heating rate has to be sufficiently fast to shift the ferrite recrystallization above the Ac1 temperature. The critical heating rate depends on the steel composition, the amount of cold-rolling reduction and the initial microstructure, as shown e.g. by processing maps produced by some authors [2,53]. In this latter case, there is no general agreement regarding how the austenite transformation and the ferrite recrystallization interact.

There are several interpretations to explain the faster transformation kinetics during faster heating. Some studies report that the presence of non-recrystallized and recovered ferrite would accelerate the austenite transformation [2,24,27,29]. The defects in the deformed ferrite grains would provide nucleation sites, fast diffusion paths and increased driving force. On the contrary, other studies do not report that the deformed ferrite would transform particularly fast [26]. According to [25], the austenite nucleation would even be difficult at the moving boundaries of the recrystallizing ferrite. According to other studies, the faster austenite transformation on faster heating would come from an increased driving force, which would

75 increase the density of austenite nuclei [23,25]. In return several studies report that newly
76 formed austenite slows down the ferrite recrystallization [22,24,29,51,54], for instance by
77 consuming potential nucleation sites [22].

78 The origin of the transition from the necklace to the banded morphology is also discussed.
79 According to [27], the austenite would inherit the initial elongated shape of the deformed
80 ferrite grains. The recrystallizing ferrite grains would also adopt this shape according to [27].
81 Other studies [24,29] mention the influence of Mn microsegregation bands stimulating the
82 austenite transformation and slowing-down the ferrite recrystallization. Li et al. [26] mention
83 the influence of the distribution of the carbides in the initial microstructure. This distribution
84 would be modified when recrystallization processes occur. According to [23,25], faster
85 heating shifts the austenite nucleation to the pearlite islands to the detriment of the slower-
86 transforming ferrite matrix. The pearlite islands would thereby confer their initial elongated
87 and banded shape (due to the cold-rolling) to the forming austenite.

88 Hence, despite a number of studies, the transition from the necklace to the banded
89 morphology remains to be understood, as well as the faster transformation kinetics during
90 faster heating. The present study aims to investigate further these issues by several means. A
91 steel with composition Fe-0.1C-1.9Mn-0.2Cr-0.2Si wt.% with cold-rolled ferrite-pearlite
92 initial microstructure is considered. A new experimental approach [55] is utilized to establish
93 in situ by synchrotron high energy XRD the austenite transformation and the ferrite
94 recovery/recrystallization global kinetics, in one single experiment. Three heating rates before
95 isothermal annealing at 800°C are applied, fast (30 and 100°C.s^{-1}) and slow (3°C.s^{-1}) to
96 induce strong or weak interactions. Only three annealing treatments are thus considered, but
97 the microstructure evolutions are observed in detail by systematic SEM characterizations,
98 focusing on the interactions of the austenite transformation with the ferrite recrystallization
99 and the carbides ripening. Particular emphasis is also put on the influence of the isolated

cementite carbides on the austenite transformation and morphogenesis. Their spatial and size distribution evolutions are established thanks to quantitative metallography, before and after ferrite recrystallization. Enrichments of the cementite carbides in Mn during annealing were already established in this steel by TEM-EDS in [49]. On this basis and from quantifications of the initial microstructure, DICTRA simulations are setup in order to understand the influence of the heating rate on the austenite transformation kinetics.

2 Studied material, experimental techniques, thermodynamic calculations

2.1 Studied material

The composition of the studied steel is given in Table 1. It is a low-carbon steel without microalloying elements (Ti, Nb, V, B). The material has been provided by ArcelorMittal either in hot-rolled or in cold-rolled state, as flat sheets of respectively 3 mm and 1.2 mm thickness. The industrial hot-rolling process consists of a reheating of the slabs at ca. 1200°C, a finish rolling at 900°C and a coiling at about 550°C after fast cooling on a run-out table. After coiling, cooling rate of the hot-rolled coils is about 20°C/h, from 550°C down to room temperature. In hot bands, the resulting microstructure is a mixture of ferrite and pearlite. The reduction ratio of the cold-rolling is 60%; this corresponds to a mean deformation of 106% in bulk. As the pearlite shows a higher flow stress than the ferrite, the deformation is even higher in the ferritic matrix. According to micromechanical models [56,57], the deformation in pearlite and ferrite is respectively equal to 67% and 119% accounting for their respective volume fractions (values are presented in Section 3.1.1).

The steel presents micro-segregations bands resulting from the processing. According to WDS measurements (spatial resolution ca. 1 μm) in the cold-rolled state, the Mn concentration along the whole thickness of the sheet ranges between 1.84 and 2.02 wt.% The chromium concentration ranges between 0.17 and 0.22 wt.% and the concentration of the

124 silicon ranges between 0.20 and 0.24 wt.%. The average spacing between the
125 microsegregation bands is of the order 4.5 μm.

	C	Mn	Cr	Si
weight fraction (%)	0.1	1.91	0.195	0.205
u-fraction (%)		1.94	0.209	0.407

126 Table 1. Chemical composition of the investigated steel. u-fractions correspond to the chemical compositions
127 with respect to the sole substitutional elements.

128 **2.2 Annealing schedules**

129 The model heat treatment, which is applied to the cold-rolled material, comprises two steps:
130 the cold-rolled samples are heated from room temperature to the annealing temperature of
131 800°C, followed by 10 min holding before helium quenching. Three constant heating rates are
132 considered: $3°C.s^{-1}$, $30°C.s^{-1}$ and $100°C.s^{-1}$. Both lowest heating rates are representative of
133 present-day annealing capabilities by most steelmakers.

134 Interrupted treatments between Ac1 and 800°C and spaced out by 10°C are done to follow in
135 detail the development of the austenite microstructure and the ferrite recrystallization. Except
136 for the XRD in situ experiments (Section 2.7), the heat treatments have been performed with
137 an in-house Rapid-Cycle Dilatometer. Heating is achieved by four light bulbs of 1500 W and
138 cooling is achieved by helium blowing.

139 **2.3 Metallographic preparation**

140 Samples prepared for SEM observations were coated with epoxy resin (sagittal cut), polished
141 with silicate grid paper down to 1 μm and finished with a colloidal silica suspension solution.
142 Before etching, an ultra-sonic cleaning bath in warm methanol (~30 min.) permits to remove
143 the fine colloidal silica particles and to avoid pollution of the samples. Two types of etching
144 have been applied. A Picral solution at 2% was used to characterize the carbides sizes and
145 distributions (initial hot-rolled or cold-rolled state or heating below Ac1). A Dino etchant (40
146 mL of distilled water, 100 mL of hydrogen peroxide (30%), 4 g of oxalic acid, 2 mL of

147 sulfuric acid and 1.5 mL of hydrofluoric acid) was used to reveal the carbides and the
148 martensite (previously austenite) after heating above Ac1 and quench. The Dino etchant also
149 permits to reveal the grain and sub-grain boundaries in the ferrite.

150 **2.4 SEM microstructural observations**

151 Two SEMs have been used in this study. The carbides microstructures were characterized
152 (heating below Ac1, Picral etching) with a Philips XL-30 FEG-SEM. The austenite
153 microstructure evolutions (heating above Ac1, Dino etching) were followed with a JEOL
154 JSM-IT300 Tungsten SEM. All observations were made in secondary electron mode. The
155 micrographs were acquired at quarter thickness of the sheets to avoid skin effects and possible
156 macro-segregation in the center. The microstructures have been observed only in the samples
157 heated at $3°C.s^{-1}$ and $30°C.s^{-1}$.

158 **2.5 Image analysis**

159 Mean pearlite island and ferrite grain sizes were measured using the intercept method defined
160 by the ASTM standard E112-96 procedure [58]. The fractions of austenite or pearlite islands
161 were quantified following the ASTM E65 standard [59]. Fractions of austenite were measured
162 after Dino etching on SEM micrographs by applying a threshold in grey levels. Fractions of
163 recrystallized ferrite were estimated following the point counting method for the $30°C.s^{-1}$
164 heating rate and by EBSD analysis based Grain Orientation Spread (GOS) parameter at $3°C.s^{-1}$
165 [60].

166 ImageJ software was used to characterize the carbides morphologies, sizes and densities. First
167 operation is a binarization of the SEM micrograph obtained after Picral etching. Despite the
168 good initial contrast, the definition of a simple threshold was not sufficient. Classical routines
169 such as opening, eroding or closing led to biases. Specific routines were developed in
170 particular to deal with the presence of grain boundaries. The reader is referred to [61] for a

171 detailed presentation. The true cementite particles sizes distribution was determined by
172 applying the Johnson-Saltikov stereological correction [62], as detailed in [63], which also
173 reviews and compares other existing correction methods.

174 **2.6 Transmission electron microscopy**

175 The chemical composition of the carbides was measured by EDXS in TEM. The specimens
176 were ground parallel to the initial faces of the flat products down to a thickness of 60 µm with
177 grinding papers, to avoid both the decarburized layer close to the surface, and
178 macrosegregations near the center. 3 mm diameter foils were punched out and then drilled by
179 electropolishing using a perchloric-acetic acid solution at 18°C with a tension of 30V. A
180 JEOL TEM microscope was operated at 200 kV (ARM FEG). Composition measurements
181 were performed with a BRUKER XFlash EDXS Silicon Drift Detector with a resolution of
182 127 eV and a collector plate of 30 mm^2. The probe size for these measurements is about 1 nm.
183 As the detection of light chemical species like carbon is not possible by EDXS because of the
184 energy resolution and pollution issues, only the major substitutional species were considered:
185 Fe, Mn, Cr and Si. By using standard statistical techniques, the relative error in the measured
186 concentrations does not exceed 5%.

187 For each investigated condition, about 5 cementite particles have been observed in detail by
188 measuring composition profiles with a probe size of ca. 1 nm. Average compositions were
189 also measured in about 20 other carbides. All particles were located in pearlite islands (not at
190 ferrite grain boundaries). It was not possible to determine with certainty whether or not the
191 particles were located in microsegregation bands. More details on the TEM sample
192 preparation and observations can be found in reference [49], which is focused on the
193 evolutions of the carbides compositions.

194

2.7 High Energy X-Ray Diffraction

The HEXRD experiments were carried out at the Deutsches Electronen-Synchrotron on the PETRA III P07 beamline (DESY, Hamburg, Germany). It was operated with a powder diffraction setup in transmission, similar to the one used in reference [64]. The samples were lamellar with dimensions 10 x 5 x 1.2 mm^3. Like for other analyses, these were cut down from the industrial steel sheet. The long direction (10 mm) corresponds to the rolling direction. The thickness (1.2 mm) direction is normal to the plane of the sheet. The X-Ray beam crosses the sample along its thickness. The size of the high energy monochromatic beam (energy 100 keV, wavelength 0.012398 nm) was 400 × 400 μm^2 broad, which means that approximatively 50,000 grains were scanned through the thickness (1.2 mm) of the sample (but the number of diffracting grains in Bragg reflection condition is lower). Calibration was performed using Fit2D software (v18, ESRF, Grenoble, France) [65,66] to adjust the sample to detector distance and correct the detector tilts using LaB6 powder. The distance was set to 1.251 m to observe fully the 6 first diffraction rings of ferrite. The diffraction patterns can be recorded at a high rate (10 Hz) on a PerkinElmer 2-D plate detector thanks to the brilliance of the line and the energy used. The thermal cycle was performed in a modified Bähr 805 A/D (TAinstruments) dilatometer. The sample could not be rotated during the experiments, but it will be seen that powder diffraction conditions could be achieved, despite the strong texture introduced by the cold rolling.

The continuous heating step was recorded in fast acquisition mode (10 Hz). Slow mode was re-activated after 60 s holding at 800°C until the end of the treatment. In slow mode, patterns are acquired every 3 s (~0,33 Hz). The temperature was measured in real time with a K-type thermocouple spot welded at the surface of the sample, just above the volume crossed by the beam. During heating in fast mode, the uncertainty in the temperature is estimated as $\Delta T = \pm 0.1 \times HR$, where HR is the heating rate and 0.1 s is the duration of an acquisition in fast

mode. For instance, uncertainty due to the acquisition method in temperature during heating at 30°C.s^{-1} is ±3°C.

A Rietveld analysis [67] was conducted to determine the phase transformation kinetics. Pictures of Debye-Scherrer (DS) rings were integrated using the Fit2D software. The 1D diffraction pattern was then refined with Fullprof software (V2.05, ILL, Grenoble, France) in a 2θ range from 2.70° to 8.70° using Pseudo-Voigt functions [68]. Only two phases have been considered (ferrite and austenite); peaks due to cementite could be detected, but these peaks were too small to allow a proper quantification. The minimum detectable austenite mass fraction is about 2% with such a procedure. This value corresponds to the accuracy of the phase fraction measurement [64].

A new method has been introduced recently to track in situ by HEXRD the recrystallization kinetics, together with the phase transformation kinetics [55]. This method is related to the presence of individual spots of intensity inside the Debye-Scherrer diffraction rings, which are ascribed to the new recrystallizing ferrite grains. By counting the number of diffraction spots, it is possible to estimate the recrystallization kinetics. The accuracy of the method has to be improved, but first comparisons with recrystallized fractions determined by EBSD are satisfactory.

2.8 Thermodynamic and kinetic simulations

The thermodynamic calculations were performed with Thermocalc software and the TCFE7 database. The kinetics simulations were performed with DICTRA software with TCFE7 and MOBFE2 databases.

3 Results

3.1 Microstructure evolutions before the austenite transformation

3.1.1 Hot-rolled microstructure

Figure 1 shows SEM micrographs of the as received industrial hot-rolled (HR) and cold-rolled (CR) microstructures. The micrographs were binarized with the procedure described in Section 2.5. After HR and subsequent cooling, the microstructure consists of polygonal ferrite and pearlite islands containing lamellar cementite carbides. The cementite is often not perfectly lamellar and presents a more rounded shape near the pearlite island boundaries. The proeutectoid ferrite grains are equiaxed and their mean radius is estimated to 5 μm. The pearlite islands have a volume fraction estimated to 16%. Observations at a larger scale (not shown here) show that the pearlite islands are often organized in bands parallel to the rolling direction. This topology is due in part to the Mn microsegregations; it is known that proeutectoid ferrite forms preferentially in Mn-depleted zones during the coiling. But in many other observations, the pearlite islands are more randomly distributed.

Important feature of the HR microstructure is the presence of a large number of isolated cementite carbides located mainly at the boundaries of the proeutectoid ferrite grains and outside the pearlite islands. Most of these carbides have an elongated shape along the ferrite grain boundaries (GBs), but some are more equiaxed. Despite their low volume fraction, the isolated carbides contain about one third of the carbon of the steel (64%). This proportion is deduced from the volume fraction of the pearlite islands (16%), which is lower than a value of 25%, expected from a thermodynamic analysis of pearlite transformation detailed in [49]. It will be seen in the following that these isolated carbides will play a major role during the austenite transformation even if presence of intergranular carbides has rarely been reported [33,40,69–72]. According to [69–71], these are formed during slow cooling before the pearlite

transformation. During the proeutectoid ferrite transformation, some carbon-rich regions of austenite would be trapped between growing ferrite grains and would then decompose to one or several cementite carbides and ferrite. Another mechanism assuming the super-saturation in carbon of the ferrite was proposed more recently in [72].

Figure 1. SEM micrographs treated by image analysis representative of the hot-rolled (a) and cold-rolled (b) microstructures. The ferrite is represented in black, the pearlitic cementite in white and the isolated carbides in red.

3.1.2 Effects of the cold-rolling

After the cold rolling (Figure 1b), the ferrite grains and the pearlite islands are flattened and elongated in the rolling direction; both are ca. 3 µm thick, while the lengths are more scattered. Inside the pearlite islands, some of the cementite lamellae remain unmodified, but most of these are now fragmented. As for the isolated carbides, those which were elongated before the CR were fragmented during the deformation, generating clusters of carbides aligned parallel to the rolling direction and distributed at the boundaries of the deformed ferrite grains (see also [26]). There are also some intra-granular carbides inside the ferrite grains, but their number is very small.

3.1.3 Microstructure evolutions during heating to Ac1

For both heating rates, 3 and 30°C.s^{-1}, the microstructure was observed (Figure 2) after heating up to 700°C and 720°C respectively. Close to the Ac1 temperature (respectively 710°C and 720°C according to microstructure observations, Section 3.4), these temperatures are representative of the initial microstructure at the start of the austenite transformation. Before this stage, different microstructural evolutions occur during the heating up to Ac1: the

recovery and recrystallization of the ferrite; the fragmentation of the cementite carbides. The latter also undergo enrichment in Cr and Mn during the slow heating at 3°C.s^{-1} [49,61]. Regarding the recrystallization, the evolutions are different for both heating rates. As shown in Figure 2a, the ferrite matrix is almost fully recrystallized after the slow heating. The recrystallized ferrite grains are nearly equiaxed and have an average size of 6 µm. Very few ferrite grains remain unrecrystallized, whereas former pearlite islands are never recrystallized. Conversely, after the fast heating, the ferrite recrystallization has almost not started (Figure 2b) at 720°C. Most ferrite grains kept their initial elongated shape resulting from the cold rolling. They contain a large number of subgrains with a typical size of 0.5 µm, which result from recovery processes starting at 380°C [55]. Hence, a transition from full recrystallization before austenite transformation to no recrystallization occurs between heating rates 3°C.s^{-1} and 30°C.s^{-1}. The order of magnitude of the critical heating rate for this transition between two modes of interaction (the so-called "weak" and "strong" interactions) is in accordance with previous studies on similar systems [2,28,73]. Detailed experimental and modelling study of recrystallization is presented in [55,74]. Regarding the pearlitic ferrite, no significant recrystallization occurs during both slow and fast heating, as confirmed by EBSD analyses.

As for the cementite carbides, different effects of the heating rate are observed for the pearlitic cementite and for the isolated carbides. The cementite carbides inside the pearlite islands undergo the same evolutions for both heating rates: they become more fragmented, leading to a more spheroidal shape and to a large increase of the particles density. They probably also undergo coarsening. Both fragmentation and coarsening phenomena are accelerated by the prior severe deformation [34,35], especially, for the fragmentation, by the defects introduced inside the cementite [36–39]. The pearlitic cementite carbides reach the same average equivalent radius, 75 nm, for both heating rates (Table 2). It should be mentioned that the lamellar carbides (i.e. not yet fragmented) were excluded from the size

measurements, which makes difficult to interpret in detail the size and densities evolutions. More measurements can be found in reference [61].

In contrast with the pearlitic cementite, the evolution of the isolated carbides (outside the pearlite islands) shows a dependence on the heating rate. During slow heating, the ferrite recrystallization, which has time to occur, modifies the size and the spatial distribution of the isolated cementite carbides with respect to the ferrite grain boundaries. Some carbides get trapped inside the recrystallized ferrite grains, while other carbides are localized at the boundaries of the ferrite grains. The latter tend to be bigger than the intragranular carbides (this could not be quantified), probably because of the faster diffusion at the grain boundaries. The mechanisms by which the recrystallization can modify the carbides distribution are discussed in Section 4.1.3. After the fast heating, the isolated carbides keep their initial distribution in the CR microstructure, mostly in the form of elongated clusters, parallel to the rolling direction and located at the boundaries of the deformed ferrite grains. There are almost no carbides inside the deformed ferrite grains (Figure 2d). The isolated carbides are larger in average after slow heating than after fast heating (Table 2), because of the larger size of the carbides located at the boundaries of the recrystallized ferrite grains. More measurements can also be found in reference [74].

Figure 2. SEM micrographs representative of the microstructure after heating to a,c,e) 700°C at 3°C.s^{-1}; b,d,f) 720°C at 30°C.s^{-1}. Figures c and d correspond to views at higher magnification of a and b. Figures e and f have been threshold to reveal carbide microstructures in both cases (carbides in bright contrast).

3.2 Ferrite recrystallization kinetics

As presented in [55], the *in situ* HEXRD experiments also allow to estimate the kinetics of the ferrite recrystallization. Figure 3 shows the recrystallized fraction as a function of the temperature during the heating stage, as determined both from HEXRD and from SEM. Above Ac1, relative fractions are plotted, that is, the ratio of the recrystallized fraction over the fraction of remaining ferrite. It can be seen that the method based on HEXRD tends to overestimate the recrystallization kinetics, compared to the image analysis of SEM micrographs. The latter are actually accurate only for the heating rate 3°C.s^{-1}, for which EBSD was employed to draw Grain Orientation Spread maps. Conversely at 30°C.s^{-1}, the estimates of recrystallized fractions are based on observation of SEM micrographs after chemical etching. Nevertheless, SEM and HEXRD observations are in agreement regarding the temperature range at which the ferrite recrystallization occurs, as a function of the heating rate.

Figure 3. Fraction of recrystallized ferrite as a function of the temperature during heating at 3, 30 or 100°C.s^{-1}. Dots: HEXRD, squares: SEM at 30°C.s^{-1} or EBSD at 3°C.s^{-1}. (In the SEM analyses, the pearlitic ferrite was excluded).

Focusing on the kinetics obtained from HEXRD, at 3°C.s^{-1}, the ferrite recrystallization starts at ca. 670°C and is almost complete at 710°C, the Ac1 temperature, as will be seen in next sections. At 30°C.s^{-1}, the ferrite recrystallization starts near 730°C and finishes at ca. 780°C. This is in good agreement with the microstructure observations near the Ac1 temperature (Figure 2). At 100°C.s^{-1}, the recrystallization kinetics is shifted to higher temperatures. It finishes in less than 6 s during the isothermal hold at 800°C. Thus, as aimed when designing the treatments, the slow heating at 3°C.s^{-1} permits (almost) full decoupling of the respective kinetics of ferrite recrystallization and austenite transformation, while faster heating at 30°C.s^{-1} and 100°C.s^{-1} will give rise to strong interactions, as will be seen in the next sections.

3.3 Austenite transformation: kinetics

The austenite transformation kinetics was measured in situ by HEXRD with the method presented in Section 2.7. Figure 4 shows the Debye-Scherrer (DS) rings recorded at 650°C and 800°C during the heating at 3°C.s^{-1}, along with the integrated intensity-2θ profiles. Additional profile at 760°C is added to illustrate the start of the austenite transformation. Continuous DS rings and the expected relative intensities of the diffraction peaks are obtained thanks to the large number of diffracting grains, leading to powder diffraction conditions. At 650°C, only visible DS rings are those of the ferrite. At 800°C, these become weaker because of the lower ferrite mass fraction, while austenite rings are clearly visible. The cementite peaks are visible only at high magnification of the I-2θ profiles. The cementite mass fraction could not be quantified by our Rietveld method.

Figure 5a shows the austenite fraction as a function of the temperature during the heating stage. According to the HEXRD, the Ac1 temperature is equal to 710°C, 740°C and 746°C respectively at 3°C.s^{-1}, 30°C.s^{-1} and 100°C.s^{-1}. (The first detection of austenite by HEXRD corresponds to the beginning of the curve). At 3°C.s^{-1} and 30°C.s^{-1}, the austenite fraction follows a similar evolution as a function of the temperature, with an upward shift of about 10°C at 30°C.s^{-1}. Hence, the phase transformation kinetics is about ten times faster at 30°C.s^{-1} than at 3°C.s^{-1}. Both kinetics show two stages: a first sluggish stage up to about 740°C and 750°C at 3°C.s^{-1} and 30°C.s^{-1} respectively, followed by a fast kinetics. During the first stage, the fraction of austenite remains below a few percent, but the austenite is clearly detected by the HEXRD. The kinetics at 100°C.s^{-1} exhibits one single stage; the fraction of austenite at any given temperature is almost always higher than at 3°C.s^{-1} and 30°C.s^{-1}. This shows that the kinetics is the fastest for this heating rate. One has though to mention that at 100°C.s^{-1}, the experimental uncertainty on the temperature is equal to ±15°C. For all heating rates, the austenite fraction remains far below the orthoequilibrium (OE) value, up to 800°C.

386 The austenite fraction evolution during the isothermal annealing at 800°C is plotted in Figure
387 5b. For all heating rates, the transformation kinetics firstly slows down quickly; the austenite
388 fraction then progressively stabilizes to reach some plateau. The higher the heating rate, the
389 faster the kinetics and the higher the final fraction of austenite. At 30°C.s^{-1} and 100°C.s^{-1}, this
390 final fraction exceeds the value expected from overall thermodynamic equilibrium. Similar
391 overshoot above the equilibrium at higher heating rates was also reported in [2,24,26,27,29].

392

393 Figure 4. 2D Debye-Scherrer rings recorded at 650 and 800°C during heating at 3°C.s^{-1}. Intensity-2θ profiles
394 from circular integration of the DS rings at 650, 760 and 800°C.

395

396 Figure 5. Austenite mass fraction as a function of a) temperature during heating; b) time during isothermal
397 annealing at 800°C (zoom on first stages in the insert). Time scale starts at the beginning of the isothermal
398 annealing in b). The dots indicate the austenite fraction at the start of the isothermal annealing.

399

400

401 **3.4 Austenite transformation: microstructure evolutions above Ac1**

402 The nucleation sites of the austenite and the different stages of its morphogenesis are
403 identified here with SEM observations of the microstructure after interrupted treatments
404 (Section 2.2). The most relevant observations are summarized here, but additional
405 observations are reported in the discussion on the austenite morphogenesis (Section 4.1).

406 **3.4.1 Slow heating, 3°C.s^{-1}**

407 Figure 6 shows SEM micrographs of the microstructure at the main stages of the austenite
408 transformation during the slow heating. The ferrite matrix is almost fully recrystallized when
409 the austenite transformation starts as already discussed and shown in Figure 4a. Outside the

410 pearlite islands, the microstructure mostly consists of large and equiaxed ferrite grains. The
411 nucleation of the austenite starts between 700°C and 710°C, at isolated carbides located at the
412 boundaries of these ferrite grains (Figure 6a). Second main nucleation sites are the boundaries
413 of the pearlite islands. Nevertheless, nucleation starts later on these sites, between 710 and
414 720°C. This first detection of austenite is in good agreement with the Ac1 determined by
415 HEXRD (710°C).

416 Up to 730°C, the growth of the austenite grains remains sluggish and limited to the
417 boundaries of the ferrite grains or the pearlite islands (Figure 6b). Austenite fraction remains
418 below 1.5%$_m$ (XRD). The austenite morphology is either spheroidal (especially when it
419 nucleated at triple junctions involving or not a pearlite island) or elongated, as a result of the
420 preferential austenite growth along the grain boundaries. At ca. 740°C, the pearlite islands
421 start to transform quickly to austenite; their transformation is almost complete at 750°C
422 (Figure 6c). Newly formed austenite grains inherit the width of the pearlite islands, typically 3
423 µm, and their high carbon concentration, 1.78 at.%. Hereafter, the austenite grains stemming
424 from the pearlite islands will be referred to as carbon-rich austenite (CRA) grains. On further
425 heating, the CRA grains grow towards the surrounding ferrite. The pearlite islands
426 transformation corresponds to a marked increase of the rate of austenite formation (Figure
427 5a). The austenite grains which nucleated on the isolated carbides grow more slowly along the
428 proeutectoid ferrite grain boundaries. Nucleation on the isolated carbides is progressive and
429 the sizes of the austenite grains nucleated on these sites are thus scattered. The austenite
430 eventually decorates the ferrite grain boundaries, giving rise to the necklace morphology.

431 At 800°C, the necklace morphology is clearly observable; most of the ferrite grain boundaries
432 are decorated by the austenite. The austenite films actually percolated before, at ca. 780°C
433 (corresponding micrograph is not shown here). The austenite films observable at 800°C grew
434 into the interior of the ferrite grains and reached a thickness of ca. 500 nm. Besides, the

austenite grains stemming from the pearlite islands achieve a banded morphology, because of the initial distribution of the pearlite islands.

Figure 6. SEM observations (Dino etching) of the microstructure after heating at 3°C.s^{-1} followed by quench up to a) 710°C; b) 730°C; c) 750°C; d) 800°C. In a), the arrows show the first grains of austenite.

3.4.2 Fast heating, 30°C.s^{-1}

During the fast heating, the austenite transformation starts in a microstructure which is almost non-recrystallized, contrary to the case of the slow heating. As shown in Figure 7a at 740°C, most of the ferrite grains are still deformed and filled with subgrains; only few recrystallized ferrite grains can be observed. Despite the different initial microstructure, the nucleation sites of the austenite remain the same as during slow heating. The austenite nucleates first on isolated carbides between 710 and 720°C (high-magnification micrographs are not shown here) and then at the boundaries of the pearlite islands (between 720 and 730°C). The Ac1 temperature determined by HEXRD is higher (740°C), but for a heating rate of 30°C.s^{-1}, this corresponds to 1 s during the experiment. What differs compared to the slow heating is the distribution of the austenite nucleation sites outside the pearlite islands. The isolated carbides are located at the boundaries of the deformed and elongated ferrite grains. The austenite grains nucleating on these sites grow equiaxially exclusively; in contrast with the slow heating, preferential growth along the grain boundaries is rarely observed, as shown for instance at 740°C in Figure 7a.

Like in the case of the slow heating, the pearlite islands start to transform at a sluggish rate before an acceleration at about 750°C, whereas the austenite grains nucleating on the isolated carbides nucleate more progressively and grow more slowly. The pearlite islands transform in

most part in a narrow temperature range, between 750 and 760°C (Figure 7b). This temperature range is slightly shifted to higher temperatures (ca. 10°C), compared to the slow heating. When the pearlite islands are fully transformed, significant recrystallization has still to take place (fraction of ferrite remaining to recrystallize depends on the experimental method, HEXRD or SEM, see Figure 3). This further recrystallization of the ferrite will contribute to the morphogenesis of the microstructure.

Figure 7. SEM observations (Dino etching) of the microstructure after heating at 30°C.s^{-1} followed by quench up to a) 740°C; b) 760°C; c) 770°C; d) 800°C. The arrows indicate: first austenite grains in (a); alignments of austenite grains at the boundaries of elongated recrystallized ferrite grains in (c).

Upon further heating up to 800°C, the microstructure undergoes simultaneous evolutions: the growth of the newly formed carbon-rich austenite (CRA) grains stemming from the pearlite islands, the nucleation and growth of the austenite grains from the isolated carbides and the recrystallization of the ferrite. All of the three processes contribute to form the banded morphology. The CRA grains grow into the surrounding ferrite matrix. Like for the slow heating, they reach at 800°C a banded morphology, which is inherited from the initial distribution of the pearlite islands. The austenite grains nucleated on the isolated carbides grow first equiaxially and then tend to impinge and to form alignments parallel to the rolling direction. Examples of such alignments are shown in Figure 7b. This distribution in bands comes from the layout of the isolated carbides in the initial microstructure, which is caused by the cold rolling.

The recrystallizing ferrite grains reach a more elongated shape than during slow heating; their length can reach 10 µm. This is the consequence of the concomitant austenite transformation, because the ferrite recrystallization is confined inside the forming bands of austenite (stemming from pearlite islands or from the isolated carbides). Thus, the new recrystallized ferrite grains inherit the initial elongated shape of the deformed ferrite grains. Figure 7c (770°C) shows several examples of elongated recrystallized ferrite grains. These are surrounded by austenite grains emanating either from perlite islands or from isolated carbides. Once the recrystallized ferrite grains have acquired an elongated shape, the austenite continues to nucleate and grow at their boundaries, thereby reinforcing further the banded topology of the microstructure. These combined phenomena lead to the banded morphology of the austenite, which is clearly observable at 800°C (Figure 7d).

3.4.3 Isothermal annealing at 800°C

During isothermal annealing at 800°C for 10 min., the austenite transformation progresses further. As shown in Figure 5c, the austenite mass fraction increases from 47% to 81% after heating at $3°C.s^{-1}$, from 49% to 85% after heating at $30°C.s^{-1}$ and from 56% to 89% at $100°C.s^{-1}$. This further growth of the austenite into the ferrite (originating from pearlite islands or isolated carbides) is associated with a disappearance of the austenite topology (Figure 8), which was initially either necklace or banded. The austenite distribution becomes more homogeneous. This vanishing of the initial morphology is already observable after 60 s of isothermal hold (corresponding micrographs are not shown). After the isothermal annealing for 600 s, there is no clear difference between the microstructures corresponding respectively to the slow and to the fast heating. In both cases, the smaller ferrite grains are fully consumed, while the largest ones remain in the final microstructure. As for the kinetics characterizations, which showed a marked slowdown of the kinetics after 60 s annealing (cf. Figure 5b), this was confirmed by SEM micrographs.

Figure 8. SEM observations (Dino etching) of the microstructure after heating up to 800°C and isothermal annealing for 600 s. a) 3°C.s^{-1}; b) 30°C.s^{-1}.

4 Discussion

4.1 Austenite morphogenesis, banded or necklace

4.1.1 Proposed mechanism

As usually reported in literature, slow and fast heating lead respectively to necklace and banded microstructures, which are established by different sequences schematized in Figure 9. During slow heating (3°C.s^{-1}), the ferrite recrystallization is almost complete before the start of the austenite transformation. At the Ac1 temperature, 700-710°C, only few ferrite remains unrecrystallized. The recrystallized ferrite grains have a size of ca. 6 µm and an equiaxed shape; many coarsened carbides are located at their boundaries because of the recrystallization process. The austenite nucleates on these carbides and then grows preferentially along the boundaries of the recrystallized ferrite grains, thereby forming the necklace morphology. Meanwhile, the pearlite islands transform to carbon-rich austenite (CRA) grains, which then grow towards the surrounding ferrite. The CRA grains have a banded morphology because of the elongated shape of the initial pearlite islands (Figure 1b, Figure 2a). The final topology of the microstructure is nevertheless dominated by the network of Austenite Nucleated on isolated Carbides (ANC) covering the ferrite grains boundaries (even if the respective fractions of ANC and CRA appears similar in the micrographs). Indeed, the initial pearlite islands occupy only 16% of the volume fraction in the initial microstructure.

530 During fast heating (30°C.s^{-1}), the recrystallization has almost not started at the Ac1
531 temperature (710-720°C). On heating, the isolated carbides thus kept their initial distribution
532 resulting from the cold rolling. It consists of clusters aligned in the rolling direction and
533 located at the boundaries of the deformed ferrite grains. Alignments of austenite grains
534 nucleate on these carbides (ANC) and grow equiaxially. By impinging, these grains start to
535 form the banded morphology. Meanwhile, the transforming pearlite islands (CRA grains) also
536 contribute to form the banded topology. The concomitant ferrite recrystallization is now
537 confined between the forming bands of austenite, originating either from the isolated carbides
538 or from the pearlite islands. Hence during fast heating, the new recrystallized ferrite grains
539 acquire an elongated shape, thereby reinforcing the banded topology of the microstructure.
540 Finally, the last austenite grains nucleate at the boundaries of the elongated recrystallized
541 ferrite grains, thereby reinforcing further the morphology in bands.

542 The mechanism proposed above for the genesis of the necklace morphology during slow
543 heating is in agreement with the literature related to initial cold-rolled ferrite-pearlite
544 microstructures [2,24–27]. The nucleation of austenite at carbides located at recrystallized
545 ferrite grain boundaries is also clearly mentioned [24,26,27], except in [25]. Nevertheless, in
546 the latter study, these carbides are observable in the presented micrographs. Conversely, the
547 origin of the banded morphology has been interpreted differently [23–25,27]. As it is obtained
548 during fast heating, the austenite transformation takes place in the presence of non-
549 recrystallized ferrite grains. The point of disagreement concerns whether or not the latter
550 transform to austenite faster than the remaining of the ferrite matrix. The role of Mn
551 microsegregation bands has also been considered. This is discussed in Sections 4.1.3 and
552 4.1.4.

553

554 Figure 9. Schematic of the austenite morphogenesis depending on the heating rate.

555

556 **4.1.2 Influence of the isolated and intergranular carbides**

557 It comes out the preceding analysis that the “isolated carbides” distribution determines the
558 formation of either a necklace or a banded austenite microstructure. The isolated carbides are
559 those localized outside the pearlite islands, in the ferrite matrix (as presented in Section 3.1.1).
560 Among these carbides, only those located at ferrite grain boundaries or triple junctions
561 (intergranular carbides) play a significant role. As the austenite starts to nucleate and grow
562 from these sites, this determines the initial spatial distribution of the austenite and its further
563 morphogenesis. The same conclusion was reached, as far as we know, in only one previous
564 study, by Li et al. [26]. Minor differences concern what are the firstly activated nucleation
565 sites (the pearlite islands in [26]). In [26], intermediate heating rates were also investigated,
566 leading to an austenite microstructure intermediate between necklace and banded.

567 The role played by these carbides may seem unexpected at first sight, because of their low
568 volume fraction in the initial microstructure (see Figure 1). This is why these carbides are
569 frequently not considered in literature [33,40,69–72]. Despite their low volume fraction, the
570 isolated carbides contain (in the studied steel) about one third of the carbon. Hence, a similar
571 proportion of the austenite is expected to form from these carbides. Contrary to the case of the
572 pearlite islands, their spatial distribution with respect to the ferrite grain boundaries may
573 evolve during heating, depending on the heating rate, because of some interaction with the
574 ferrite recrystallization (see next section). Conversely, the pearlite islands and the austenite
575 resulting from their transformation keep a banded morphology whatever the heating rate.
576 However, the pearlite islands have an initial volume fraction equal to 16%, which limits their
577 impact on the final microstructure.

In order to confirm the role played by the isolated carbides, SEM observations were conducted. Figure 10 shows some examples for a heating up to 740°C at 3°C.s^{-1}. In most cases, a carbide (white contrast) was observed as expected inside austenite grains forming along planar ferrite grain boundaries. However, the presence of such carbide is not systematic. Despite the absence of fully conclusive observations, the preferential nucleation of austenite on isolated carbides is highly probable: combined with a ferrite grain boundary, the intergranular cementite particles represent high-energy defects, which are favorable heterogeneous nucleation sites for the austenite. The austenite grains then grow preferentially in their vicinity, because the dissolving carbides provide a source of carbon. Several studies also report that in presence of intergranular carbides, the austenite nucleates preferentially on these sites [26,27,30,32,33]. When the austenite is reported to nucleate at "empty" ferrite/ferrite grain boundaries [75–77], the considered microstructures do not include any intergranular carbide.

The only other significant nucleation sites for the austenite are the intragranular carbides, which are trapped inside recrystallized ferrite grains, mostly in the case of the slow heating. Some examples can be seen in Figure 2. However, few austenite grains nucleated on these sites; these grains grew slowly and always stabilized to a limited size (Figure 10a). Their slow growth comes most likely from the bulk diffusion which is involved; their small size comes from the absence of other neighboring carbon sources. Therefore, these intragranular austenite grains contribute weakly to the austenite morphogenesis. In the case of the fast heating, intragranular carbides were almost never observed.

Figure 10. SEM micrographs (Dino etchant) showing austenite grains nucleated on ferrite grain boundaries after heating to 730°C at 3°C.s^{-1}. Cementite carbides appear in light contrast.

4.1.3 Influence of the ferrite recrystallization

From our experimental observations, we have established in the studied steel that the main influence of the ferrite recrystallization on the austenite morphogenesis is indirect, but determining. During the slow heating, it modifies the spatial distribution of the isolated carbides which are then located in large part at the boundaries of the recrystallized ferrite grains. This is thought to be the origin of the necklace microstructure. These carbides are also larger than in the initial microstructure. The detailed interactions between the recrystallizing ferrite and the carbides are not clear from the literature. Straightforward reason for the larger intergranular carbides sizes is that the presence of the grain boundary would accelerate the diffusion and the coarsening processes. The large number of isolated carbides at the boundaries of the recrystallized ferrite grains can be explained if the carbides impeded the moving boundaries of the recrystallizing ferrite grains. According to [2,30], the boundaries of the recrystallizing ferrite grains can in some cases overcome the pinning force of the carbides and leave behind intragranular carbides, inside the new recrystallized ferrite grains. These carbides would tend to dissolve to the benefit of those localized at the grain boundaries.

During the fast heating, the ferrite recrystallization has a different effect, which comes from its interaction with the concomitant austenite transformation. As described previously, the bands of transforming austenite tend to “channel” the ferrite recrystallization, which reinforces the banded morphology. Same observation was reported in [24]. In return, the ferrite recrystallization has an impact on the austenite morphogenesis. Alignments of austenite grains form at the boundaries of elongated recrystallized ferrite grains (Figure 7c). Similar observation was reported in [27].

Point of disagreement with some previous studies [24,27] is related to the rate of transformation to austenite of the deformed and non-recrystallized ferrite grains. During fast heating, this would explain the morphogenesis in bands according to these works. The

austenite grains would acquire a banded morphology by inheriting the elongated shape of the deformed ferrite grains [27]. The fast transformation of the deformed ferrite grains is explained in [24,27] by the energy stored inside and by the defects, which provide nucleation sites and fast diffusion paths. However, in present study, any faster transformation of the deformed ferrite could not be seen clearly from the microstructural observations. Further quantitative analysis of the microstructure would be necessary, as done for instance in [24]. Let us mention that in the latter study, the non-recrystallized ferrite grains contained a large number of intragranular cementite carbides. This may explain in part their fast transformation to austenite. Conversely in present study, the deformed ferrite grains were almost empty of any carbide (Section 3.1.3).

Let us mention that the development of the banded morphology was interpreted in [25,27] without considering any influence of the deformed ferrite grains on the austenite transformation. For very fast heating rates, 100°C.s^{-1} in [25] and 140-693°C.s^{-1} in [27], the austenite transformation takes place exclusively from the pearlite islands, which confer their elongated shape to the austenite. In the ferrite matrix, the more sluggish austenite transformation has not enough time to occur. Hence, in these cases, the morphology in bands comes from the selection of the nucleation sites for kinetic reasons. This selection of austenite nucleation sites (pearlite vs. ferrite grain boundaries) was also been put into evidence in [23]. Such transition did not occur in present study because of the too slow heating rates considered.

4.1.4 Influence of the Mn microsegregation bands

The investigated steel contains manganese microsegregation bands (Mn bands) aligned with the rolling direction (Section 3.1.1). Although the range of Mn concentrations is low (1.8-2.0 wt.% at quarter thickness, according to WDS) possible impact on the morphogenesis in bands during fast heating cannot be ruled out. No clear correlation could though be found between

653 the spacing of the Mn bands (4.5 µm according to WDS) and of the austenite bands after fast
654 heating at 30°C.s^{-1}, for instance up to 800°C (Figure 7d). The austenite bands are actually
655 scattered, which makes difficult to measure their spacing. In contrast, in [24] where a steel
656 with higher magnitude of Mn concentrations was considered, the bands of austenite were
657 better defined and more continuous.

658 More indirect impact of the Mn bands, could be to influence the distribution of the cementite
659 in the initial microstructure. In [24], it is reported that the Mn bands are spatially correlated
660 with a higher density of intragranular carbides, inside the deformed ferrite grains. In [2], it is
661 also mentioned that the pearlite in the initial microstructure tends to occupy the Mn-rich
662 regions. Weaker impact of the Mn bands on the initial pearlite distribution was found in
663 present study (Section 2.1). This may come again from the weak degree of Mn segregation in
664 the investigated steel.

665

666

667 **4.2 Austenite transformation kinetics**

668 **4.2.1 Kinetics stages; identification of two sub-systems**

669 For both heating rates 3°C.s^{-1} and 30°C.s^{-1}, the austenite transformation starts at a sluggish
670 rate (Figure 5b), before a strong acceleration at about 740 and 750°C respectively. (The first
671 stage is less visible at 100°C.s^{-1}, but this may come from the precision of the measurements).
672 This first stage corresponds to the slow growth of the first austenite grains, which nucleated
673 both at isolated carbides and at the boundaries of pearlite islands. The acceleration
674 corresponds clearly to the transformation of the pearlite islands, according to the SEM
675 micrographs (Section 3.4). The impact on the global kinetics is visible because the pearlite
676 islands transform simultaneously in a narrow temperature range of about 10°C. In contrast,

677 the austenite grains stemming from the carbides isolated in the ferrite matrix nucleate and
678 grow more progressively and more slowly. Their impact on the global kinetics is thus less
679 visible. Hence, two sub-systems behaving differently in terms of kinetics are identified: the
680 austenite stemming from the pearlite islands (carbon-rich austenite 'CRA'), or the isolated
681 carbides (austenite nucleated on carbides, 'ANC').

682 Conversely to previous studies which also considered an initial ferrite-pearlite microstructure
683 (e.g. [1,76]), there is no sharp transition from a fast regime of pearlite transformation followed
684 by a slower ferrite / austenite transformation. This is due to the isolated carbides, which
685 dissolve progressively, both before and after the pearlite islands transformation. Moreover, as
686 the pearlite islands occupy initially 16% of the volume fraction, their transformation does not
687 make increase drastically the austenite fraction (Figure 5b). Once the pearlite islands have
688 fully transformed at 750 or 760°C, the austenite transformation goes on in both sub-systems,
689 without further identifiable kinetics stages.

690

691 **4.2.2 Influence of the heating rate**

692 The faster the heating rate, the faster the austenite transformation kinetics, during both the
693 heating stage and the subsequent isothermal hold. During heating, the austenite
694 transformation is about ten times faster at 30°C.s^{-1} than at 3°C.s^{-1}; it is even faster at 100°C.s^{-1}
695 (Section 3.3). These results from XRD are further confirmed by austenite fractions
696 determined by image analysis at 800°C: 49% at 3°C.s^{-1}, 49% at 30°C.s^{-1} and 47% at 100°C.s^{-1}
697 . Similar observation was done in previous studies regarding the isothermal annealing stage
698 [2,23–27,29]. As for the heating stage, there is no clear agreement in the literature, but some
699 studies do also report faster transformation during faster heating (e.g. [2,24]). Three possible
700 origins of the faster kinetics are discussed in the following: the presence of non-recrystallized

ferrite, the higher driving force linked with the faster heating and the faster growth of the austenite stemming from the pearlite islands. (The influence of kinetics regimes of austenite growth involving or not the partition of the alloying elements is treated separately in the next Section).

According to some studies [2,24,29], one possible origin of the faster austenite transformation during faster heating and/or subsequent holding is the presence of non-recrystallized ferrite grains, which would transform faster to austenite. In present study, this would explain the faster kinetics at 30°C.s^{-1} than at 3°C.s^{-1}, because for the latter heating rate, the ferrite almost fully recrystallizes before reaching the Ac1 temperature. As mentioned in Section 4.1.3, faster transformation of the non-recrystallized ferrite is possible in the investigated steel, but further quantitative microstructural characterization would be necessary to confirm this. Let us mention that for both heating rates 30°C.s^{-1} and 100°C.s^{-1}, the ferrite recrystallization is concomitant to the austenite transformation (Section 3.2). Hence, the faster austenite transformation kinetics at 100°C.s^{-1} than 30°C.s^{-1} can be less clearly interpreted by the presence of more non-recrystallized ferrite than when comparing heating rates 3°C.s^{-1} and 30°C.s^{-1}. At least, accelerated growth in non- recrystallized ferrite is not the sole mechanism.

Other possible origin of the faster austenite transformation kinetics is that during faster heating, the nucleation would be shifted to higher temperatures, increasing thereby the driving force and the density of the austenite nuclei. The transformation kinetics would be increased by the higher density of growing fronts of austenite. Such refinement of the microstructure was put into evidence in [23] (considering a hot-rolled initial state, with two heating rates 1 and 300°C.s^{-1}). However, in present study, the austenite transformation kinetics is not shifted to much higher temperatures, according to the HEXRD experiments (Figure 5a). The transformation rate of the pearlite islands depends weakly on the heating rate. As for the

726 austenite grains forming in the ferrite matrix, their density is not evidently higher at higher
727 heating rate, according to SEM micrographs (compare Figure 6 and Figure 7).

728 The only effect of the heating rate on the austenite transformation kinetics which is
729 observable on the micrographs concerns the austenite stemming from the pearlite islands.
730 Although the transformation rate of the latter depends weakly on the heating rate (Section
731 3.4), these transform to coarse, carbon-rich austenite (CRA) grains, which then do show a
732 large difference in growth rate between both heating rates, 3 and 30°C.s^{-1}. For example, the
733 CRA grains are clearly larger at 800°C after the fast heating (Figure 11). At 760, 770 and
734 800°C (0s) the CRA grains are 3, 5 and 10 µm thick during slow heating and respectively 10,
735 12 and 14 µm thick during fast heating. This faster growth could be ascribed in part to the
736 presence of non-recrystallized ferrite, but as mentioned above, this has to be examined with
737 further quantitative microstructural analyses. As the growth of the CRA grains is thermal-
738 activated, there is thus no straightforward interpretation for their faster growth on faster
739 heating. But it explains in part the faster overall kinetics measured by HEXRD (Figure 5).
740 The growth of the CRA grains is further discussed in the modeling part, Section 4.2.3.

741

742

743

744 Figure 11. Optical micrographs of the microstructure after heating up to 800°C at a) 3°C.s^{-1}; b) 30°C.s^{-1}.

745

746 To conclude, the qualitative analysis of the microstructure evolutions is not sufficient to
747 understand why the austenite transformation is faster during faster heating. The higher final
748 fraction of austenite with faster heating also remains to be interpreted, as well as how this

749 fraction can exceed the orthoequilibrium (Section 3.3). In the following sections possible
750 outcomes of thermokinetic analyzes are examined.

751 **4.2.3 Thermokinetic analysis**

752 **4.2.3.1 Simulation approach; representation of the microstructure**

753 The austenite transformation is simulated with the DICTRA software [78], which resolves the
754 diffusion equation in a multi-component system. The simulations predict the velocity of the
755 interfaces and the evolutions of the composition profiles. The alloy is simplified here to the
756 ternary Fe-0.1C-1.91Mn (wt.%) system. As in recent works using DICTRA [30,31,43,44,53],
757 it is assumed that the only rate-limiting process is the diffusion of the alloying elements Mn
758 and C and that the local equilibrium holds at the interfaces. (Let us mention that
759 paraequilibrium [1,79] or other deviations to local equilibrium [79–81] have been considered
760 in other studies).

761 A geometrical representation is defined for both main origins of the austenite: the isolated
762 carbides and the pearlite islands. 1D simulation cells with spherical symmetry, afforded by
763 DICTRA, are utilized (Figure 12). The formation of the austenite stemming from the pearlite
764 islands is simulated in two stages: first, the transformation of the pearlite island to a carbon-
765 rich austenite (CRA) grain, then the growth of the latter towards the surrounding ferrite
766 matrix. The simulation cell representing the first stage (Figure 12a) contains a pearlitic
767 spheroidized carbide inside a ferrite matrix; the austenite grows from the exterior. (Hence, it
768 does not describe the transformation of the full pearlite island to a CRA grain, but only one
769 pearlitic carbide). Although this representation is not perfect, it includes an essential feature
770 of the process: the fast diffusion of the alloying elements from the carbide to the austenite,
771 through the ferrite. Next stage is the growth of the CRA grain towards the surrounding ferritic
772 matrix: the geometrical representation by a spherical simulation cell is straightforward (Figure

12b), although the “true” CRA grains have an elongated shape. The formation of the austenite stemming from the isolated carbides (ANC) is also well represented by a spherical simulation cell (Figure 12c). The austenite is assumed to form rapidly a shell around the carbide. The respective sub-systems or simulation cells will be denoted hereafter P, A and I. (A and P cells serve to describe the formation and then the growth of the of CRA grains; I cell describes the evolution of the ANC).

Figure 12. Spherical simulation cells employed in the DICTRA simulations. a) dissolution of a pearlitic cementite carbide (P sub-system); b) Growth of carbon-rich austenite (CRA) grain into ferrite (A sub-system); c) dissolution of an isolated carbide leading to formation of ANC (I sub-system).

Figure 13 schematizes the representation of the overall microstructure. The starting microstructure consists of pearlite islands and isolated carbides distributed in the ferrite matrix (a). Upon annealing, the austenite will consume the pearlite islands, until the formation of carbon-supersaturated austenite grains (the CRA grains) which will inherit the former pearlite grain size and carbon composition (b). This part of the simulation concerns the cell P. In a second stage, the resulting CRA grains grow into the surrounding ferrite matrix (c), as calculated in the cell A. Meanwhile, austenite transformation from isolated carbides (ANC) is described by the sub-system I. This representation has drastic simplifications: the absence of isolated carbides in the vicinity of the pearlite islands and the fact that there is no transfer of carbon between A and I sub-systems, which are considered as closed systems. Also, the isolated carbides have the same sizes and compositions, contrary to the experimental observations. Consequences of these simplifications will be discussed when comparing the simulations to the experiments.

798 Figure 13. Geometrical representation of the microstructure; two stages of austenite transformation. a) Initial
799 microstructure; b) first stage of austenite transformation; c) second stage.

800

801 The dimensions inside the simulation cells (Table 2) are based on the measurements by
802 quantitative metallography of the average sizes of the spheroidized pearlitic carbides and the
803 isolated carbides [49,61]; the pearlite islands have an average radius of 2.5 μm, which gives
804 the size of the CRA grain in cell A. The sizes of the carbides are assumed to be the same for
805 both heating rates 30 and 100°C.s^{-1}, as no measurements were done for the latter experiment.
806 The total size of cell P is set by knowing from the experiment the overall carbon
807 concentration in the pearlite islands, 1.78 at.% and then by applying a molar balance on the
808 carbon. (Carbon concentration in ferrite is close to zero). Setting the total size of cells A and I
809 (i.e. the size of the ferrite "shells") is less straightforward. Indeed, the number density of the
810 isolated carbides and of the CRA grains could not be determined accurately, due to the
811 complexity of the microstructures.

812 One possible approach could be to set the size of the ferrite shells in cells A and I such that
813 the overall carbon concentration in each cell is the one of the steel, 0.46 at.%. But it was
814 realized that a respectively higher and lower concentration should be ascribed to cells A and I,
815 to avoid large discrepancies between the simulation and the experiments. Indeed, the carbon
816 distribution is actually heterogeneous. In the initial microstructure, the pearlite islands contain
817 about two thirds of the carbon, but they occupy 16% of the volume fraction; these high
818 heterogeneities subsist during the intercritical annealing. Different criteria, such as the
819 approximate number density of the isolated carbides, guided the selection of the A and I cell
820 sizes; these criteria are detailed in [61]. As a result, the overall carbon content in cells A and I
821 was set to 0.65 at.% and 0.30 at.% respectively. The cell sizes were calculated accordingly by
822 applying carbon molar balances.

823 The cementite Mn compositions in cells P and I (Table 2) are taken from the EDS
824 measurements detailed in references [49,61]. For the heating rate at 100°C.s^{-1}, no
825 measurements were done, but it can be expected that the compositions are the same as for the
826 heating at 30°C.s^{-1}, because the latter heating rate is already too fast to permit Mn enrichment
827 in the cementite [61]. In cell A, it is assumed that the CRA grain has the average Mn
828 concentration of the steel (u^0_{Mn}=1.94%), even though the initial partition of the Mn inside the
829 cementite platelets could involve local subsisting heterogeneities (so-called ghost cementite).
830 It can be assumed that these heterogeneities are too far from the austenite/ferrite interface to
831 influence its velocity, because of the large dimensions of the cell A. In the ferrite, the Mn
832 content is calculated such that the overall Mn content has the bulk steel composition
833 (u^0_{Mn}=1.94 %) in all cells P, A and I.

834 Heatings at 3, 30 and 100°C.s^{-1} are simulated. The temperature at which the austenite starts to
835 form is taken from the experiments; values are reported in Table 2. DICTRA gives the
836 possibility to trigger the austenite transformation once some critical driving force is overcome
837 (usually 10^{-5} RT [30,82]). However, in view of the limited knowledge regarding the austenite
838 nucleation kinetics, both from present study and literature [76,77,83], setting this critical
839 driving force almost amounts to impose directly the temperature at which the austenite starts
840 to form. For each simulation cell, the same start temperature is used for all heating rates,
841 despite small differences (less than 10°C) according to the experiment. The purpose is to
842 compare more easily the three simulations.

843

Heating rate (°C.s^{-1})	**θ radius (nm)**	**Total cell radius (nm)**	**u^{θ}_{Mn} (%)**	**Start T (°C)**
3	75	203	8.8	720
30 and 100	75	203	7.2	720
Heating rate (°C.s^{-1})	**γ grain radius (nm)**	**Total cell radius (nm)**	**u^{γ}_{Mn} and u^{α}_{Mn} (%)**	**Start T (°C)**

3, 30 and 100	2500	3530	1.94	755
Heating rate (°C.s^{-1})	**θ radius**	**Total cell radius (nm)**	**u^{θ}_{Mn} (%)**	**Start T (°C)**
3	110	565	8.8	720
30 and 100	75	373	7.2	720

Table 2. Main parameters defining the DICTRA simulation cells.

4.2.3.2 Results: kinetics related to each sub-system

In the following, the simulation results are presented by focusing on the austenite transformation kinetics. Composition profiles or operative tie-lines are not presented in order to shorten the presentation; these are detailed in [61].

Dissolution of pearlite islands (system P)

Figure 14a shows the austenite volume fraction as a function of the temperature during the heating inside the cell P, representing the pearlitic carbide dissolution (Figure 12a, Figure 13b). (The cementite fraction is not plotted for clarity). For all heating rates, the transformation kinetics accelerates with increasing temperature because of the faster diffusion. The operative tie-lines and the composition profiles (not presented here) show that the Mn partitions during the transformation. Austenite transformation with partition of Mn is possible here because of the fast diffusion through the ferrite and the short diffusion distances. The simulation reproduces well the main kinetics features of the pearlite islands transformation, which were established experimentally: the fast kinetics and the weak dependence on the heating rate. Indeed, the curves are shifted only by 10°C between 3°C.s^{-1} and 100°C.s^{-1} heating rates. The temperature range for the transformation of the pearlite islands is also in agreement with the microstructure observations (at 3 and 30°C.s^{-1}).

Figure 14. Austenite volume fraction as a function of temperature according to DICTRA simulations inside the simulation cells represented in Figure 12a-b. a) transformation of the pearlite island (sub-system P); b) growth of the CRA grain (sub-system A). OE and NPLE curves represent the austenite volume fraction at equilibrium and after a ferrite to austenite transformation without partition of the Mn; c) carbon concentration profiles at 780°C in simulation cell A, as a function of the distance from the center of the simulation cell.

Growth of the CRA grains (system A)

Next stage is the growth of the CRA grain towards the surrounding ferritic matrix. The evolution of the austenite fraction inside the A simulation cell (Figure 12b, Figure 13c) is plotted in Figure 14b for all heating rates. This time, the austenite transformation occurs without partition of the Mn in all cases. (Tie-lines and Mn concentration profiles are again not presented). All simulation curves tend to follow one single curve denoted NPLE (calculated with Thermocalc), which corresponds to the maximum fraction of austenite which can be formed without Mn partition. There is an apparent discrepancy for both highest heating rates (30 and 100°C.s^{-1}), but it corresponds to a time discrepancy of less than 1 s. In fact, for heating rates 30°C.s^{-1} and 100°C.s^{-1}, the carbon has not enough time to diffuse and to reach a homogeneous concentration inside the austenite. This is illustrated in Figure 14c which shows the carbon concentration profiles calculated for instance at 780°C. However, the operative tie-line at the γ/α interface is the same one for the three heating rates; it corresponds to the NPLE regime. This is illustrated by the carbon concentration in the austenite at the γ/α interface, which is the same for the three heating rates. Due to the high carbon concentration ascribed to the cell A (see previous Section), full austenite transformation is achieved at 800°C at 3°C.s^{-1}, and in less than 2 s at 800°C after both heatings at 30 and 100°C.s^{-1}.

Dissolution of isolated carbide and growth of ANC (system I)

888 Figure 15a shows the result of the simulation for the austenite stemming from the isolated
889 carbides during the heating up to 800°C. For all heating rates, three stages can be identified.
890 The first slow stage corresponds to the carbide dissolution involving the partition of the Mn.
891 The sharp acceleration at the second stage corresponds to the shift to a regime of dissolution
892 without partition (PLE→NPLE). It occurs at the partition-no partition transition temperature
893 (PNTT [45]), which can be calculated from thermodynamic data, as presented in
894 [42,43,45,46]. The PNTT increases with increasing Mn concentration in cementite. The
895 PNTTs calculated with Thermocalc are equal to 730°C at 3°C.s^{-1} and 725°C at 30 and
896 100°C.s^{-1}. These values are in agreement with the DICTRA simulations. The last stage
897 corresponds to the final ferrite/austenite transformation. Like for the CRA grains growth, it
898 occurs without Mn partition and the austenite fraction follows again the maximum predicted
899 for this regime (NPLE curve). The discrepancy at 3°C.s^{-1} comes from the fact that significant
900 partition of Mn occurred during the first stage.

901

902 Figure 15. Austenite volume fraction evolution according to DICTRA simulations representative of the isolated
903 carbides dissolution (sub-system I). a) during heating, as a function of temperature; b) during isothermal hold at
904 800°C. OE and NPLE curves have the same meaning as in Figure 14. (Values are different because of the
905 different overall carbon concentration in cells A and I, see Table 2).

906 The ferrite to austenite transformation goes on during the isothermal hold at 800°C after all
907 heating rates (Figure 15b). In this stage, the Mn partitions from the ferrite to the austenite and
908 the kinetics is controlled by the diffusion of the Mn inside the ferrite [61]. After the heating at
909 3°C.s^{-1}, the austenite fraction slightly overcomes the equilibrium value in less than 10 s, in
910 accordance with the experiment, if taking account of the experimental uncertainties. Actually,
911 the system is not fully equilibrated, as heterogeneities in Mn concentration subsist in the
912 austenite [61]. After the heating at 30°C.s^{-1}, the austenite fraction also reaches a plateau in

913 less than 10 s, but the final fraction exceeds the OE value by ca. 10%. The discrepancy is
914 even higher at 100°C.s^{-1}. This “overshoot” of the austenite OE fraction comes from the
915 absence of Mn partition up to 800°C. As a result, there is more Mn remaining available to
916 partition from the ferrite to the austenite, and more austenite will thus be formed. Similar
917 conclusion was reached in [30]. A final stage towards the equilibration is observable for both
918 faster heatings: after ca. 100 s, the austenite fraction decreases slowly; the kinetics is then
919 controlled by the Mn diffusion in the austenite, which is about 100 times slower than in the
920 ferrite.

921 The previous kinetics simulations allow to understand why the austenite transformation
922 kinetics is faster during faster heating. One common result comes out: after the dissolution of
923 the cementite carbides (either isolated in the matrix or inside pearlite islands), the further
924 ferrite/austenite transformation always occurs without partition of Mn during the heating up to
925 800°C (for the investigated range of heating rates). As a result, the transformation kinetics
926 depends only on the temperature, because the austenite fraction follows in each sub-system
927 some maximum fraction (denoted NPLE in the curves), which is predictable from
928 thermodynamics. Consequently, faster heating leads to faster austenite transformation
929 kinetics. Accordingly, the experimental curves in Figure 5 do show kinetics which depend
930 only on the temperature, with small differences between heating rates 3°C.s^{-1}, 30°C.s^{-1} and
931 100°C.s^{-1}. Some microstructural observations are in good agreement with these simulations.
932 As presented in Section 4.2.2, the CRA grains grow faster during faster heating, according to
933 the measurements. Direct experimental confirmation is nevertheless more difficult for the
934 austenite stemming from the isolated carbides, as the kinetics specific to each carbide are
935 more scattered. Finally, the “overshoot” of the equilibrium austenite fraction during
936 isothermal hold after the fast heating comes from the absence of Mn redistribution during
937 heating after the carbides dissolution, as presented above.

4.2.3.3 Results: overall kinetics during the heating stage

The overall fraction of austenite according to the simulation, f^{γ}, is calculated in two stages, as represented in Figure 13. First stage corresponds to the simultaneous transformation of the pearlite islands and the isolated carbides.

$$f^{\gamma} = f_P^{\gamma} f_P + f_I^{\gamma} f_I \quad (1)$$

where f_P^{γ} and f_I^{γ} are the volume fractions of austenite calculated in the sub-systems P and I (the results are plotted in Figure 14a and Figure 15). f_P is the volume fraction of the pearlite islands, which is known experimentally: f_P=16% (Section 3.1.1). f_I is the volume fraction ascribed to the isolated carbide sub-system; it is calculated hereafter.

Second stage corresponds to the growth of the CRA grains into the surrounding ferrite matrix, while the austenite transformation from the isolated carbides continues.

$$f^{\gamma} = f_A^{\gamma} f_A + f_I^{\gamma} f_I \quad (2)$$

where f_A^{γ} is the volume fraction of austenite calculated in the sub-system A (results are plotted in Figure 14b) and f_A the volume fraction occupied by the sub-system A.

Assuming for simplicity that the volume and the molar fractions are equal, the carbon is distributed in A and I sub-systems according to the following molar balances:

$$r x_C^0 = f_A x_C^A \quad (3a)$$

and

$$(1 - r) x_C^0 = f_I x_C^I \quad (3b)$$

where x_C^0 is the molar carbon content of the steel, 0.453 at.%, x_C^A and x_C^I are the carbon molar concentrations in sub-systems A and I. r is the proportion of the carbon of the steel inside the A sub-system. It is equal to the proportion of carbon inside the pearlite islands in the initial

960 microstructure, because the CRA grains inherit the carbon of their parent pearlite island. *r* is
961 known from the experiments (Section 3.1.1): r=64%. The proportion of carbon inside the
962 isolated carbides is equal to (1-*r*). Both previous equations let one degree of freedom to
963 calculate f_A, f_I, x_C^A and x_C^I (knowing that $f_A+f_I=1$). As mentioned above, x_C^A and x_C^I were set to
964 x_C^A=0.65 at.% and x_C^I=0.30 at.% by following an approach detailed in [61]. From previous
965 equations, f_A=44% and f_I=56%.

966 Figure 16 shows the calculated overall austenite fraction during the heating as a function of
967 the temperature for the three heating rates 3, 30 and 100°C.s^{-1}. Four stages are visible: (i)
968 sluggish cementite dissolution in I sub-system (isolated carbides); (ii) sharp acceleration when
969 the PNTT is reached in I sub-system; (iii) pearlite islands transformation (P sub-system); (iv)
970 ferrite to austenite transformation without Mn partition (NPLE regime) in both A[1] and I sub-
971 systems. The curve denoted NPLE represents the sum of the NPLE austenite fractions inside I
972 and A subsystems ($f^{NPLE} = f_A^{NPLE} f_A + f_I^{NPLE} f_I$).

973

974

975

976 Figure 16. Overall austenite fraction as a function of temperature during heating at 3, 30 and 100°C.s^{-1} according
977 the simulation (lines) and the experiments (dots). Main stages are indicated by the arrows.

978 The simulations reproduce the main experimental tendency: the austenite fraction follows a
979 similar evolution as a function of the temperature for the three heating rates. This is

[1] The simulations in cell A are started at 749, 755 and 766°C at 3, 30 and 100°C.s^{-1} respectively, unlike the simulations presented previously (Section 4.2.2), which were started at 755°C. The three temperatures correspond to the end of the austenite transformation in cell P for the three heating rates.

particularly true above ca. 760°C, during the final ferrite to austenite transformation under NPLE regime: the three simulations are close to the "NPLE curve". Hence, despite the discrepancies with the experiments, these simulations show that the similar kinetics for the three heating rates can reasonably be explained by the partitionless growth of the austenite during the heating, once the cementite has fully dissolved. Other possible origins of the faster kinetics, such as the more intense nucleation or the presence of non-recrystallized ferrite (see Section 4.2.2) should still be investigated with more quantitative microstructural characterizations. However, the kinetic analysis presented here is likely to remain valid whatever these further improvements. It already explains in large part the kinetic trends during the heating.

Although the simulation framework introduced here allowed to interpret the influence of the heating rate on the austenite transformation kinetics, it is not yet sufficiently precise for quantitative predictions. As can be seen in Figure 16, the overall kinetics is largely overestimated (except at 100°C.s^{-1}). There are several origins:

- The simplification to the ternary Fe-C-Mn system (instead of Fe-C-Mn-Cr-Si) which makes overestimate the austenite fraction by about 5%. The Cr also strongly stabilizes the cementite by increasing the PNTT [42], even when it is a minor element of the steel, according to kinetic simulations [48].
- Considering for the isolated carbides distributions of size and Mn/Cr composition would spread their dissolution in a larger temperature range and thus slow down the calculated overall kinetics. Progressive nucleation of the austenite should also be considered, as shown by the microstructural observations. This is thought to be the main origin of the too sharp and early start of the simulations at 30 and 100°C.s^{-1}, compared to the experiment.
- The geometry of the I cell is actually no more representative once the austenite has decorated the ferrite grain boundaries to form the necklace network (see e.g. Figure 7).

The austenite then grows to the ferrite from the exterior, instead of the center of the simulation cell, as assumed currently. This low representativeness of the I simulation cell at late stages is the reason why the simulations are not compared to the experiment during the isothermal hold step. Nevertheless, the current geometrical representation already allows to predict the "overshoot" of austenite fraction above the OE value after faster heating.

Final possible improvement concerns the distribution of the carbon between the austenite stemming respectively from the isolated carbides and from the pearlite islands. A carbon concentration of 0.65 at.% and 0.30 at.% was ascribed respectively to the A and I simulation cells (Section 4.2.3.1), in order to reflect the carbon concentration heterogeneity coming from the initial microstructure. However, there is probably a transfer of the carbon from the A sub-system to the I sub-system during the heating. As seen in Figure 6 and Figure 7, the austenite grains stemming from the pearlite islands and the isolated carbides end up to percolate and to form one single network of austenite, inside which the carbon concentration will tend to homogenize. The hypothesis of closed A and I subsystems is probably too strict.

This may explain another discrepancy that we have not yet pointed out, concerning the size of the CRA grains. According to the current simulations in A cell, the CRA grains should reach for the three heating rates nearly the same size at 800°C. Indeed, the austenite fraction is nearly the same (with time shifts less than 2 s), as shown in Figure 14a. However, the observation (Figure 11) shows that the CRA grains are clearly larger after the heating at $30°C.s^{-1}$ than at $3°C.s^{-1}$. It is thought that during the slow heating, the carbon has more time to leave the CRA grains towards the austenite necklace network. The CRA grains would thus reach a smaller size, because the carbon concentration in austenite remains fixed by the equilibrium tie-line corresponding to the NPLE growth regime. Actually, this transfer of carbon from the pearlite bands to the austenite network at grain boundaries may be another

origin of the transition from the banded to the necklace microstructure when decreasing the heating rate.

Final comment regards the influence of the non-recrystallized ferrite on the austenite transformation kinetics. The defects present in the ferrite would accelerate the diffusion according to previous works [2,24,29]. According to our simulations, this is not thought to have significant consequences during the heating stage. Indeed, the austenite grows under the NPLE regime and therefore, the rate-limiting process is the diffusion of carbon inside the austenite. (As was already pointed out in reference [1], see the Figure 10). This is illustrated by the examples of carbon concentration profiles plotted in Figure 14c inside the simulation cell A. The carbon concentration in austenite has not enough time to homogenize, while it remains close to zero and homogeneous inside the ferrite. Hence, accelerating or not the diffusion inside the ferrite would not change the simulation results. During the subsequent isothermal step at 800°C, the rate-limiting process is then the Mn diffusion inside the ferrite, according to the simulations in cell I. But at this temperature, the ferrite is fully or almost fully recrystallized, according to our experiments (Section 3.2).

5 Conclusion

The austenite transformation occurring during the intercritical annealing of a dual-phase Fe-0.1C-1.9Mn-0.2Cr-0.2Si wt.% (DP-600) steel has been investigated. The initial microstructure is ferrite-pearlite cold-rolled to 60% amount of reduction. Three heating rates have been applied, slow (3°C.s^{-1}) and fast (30 or 100°C.s^{-1}) before an isothermal holding at 800°C, to induce weak or strong interactions between the austenite transformation, the ferrite recrystallization and the cementite carbides ripening. Main conclusions are the following:

- The initial microstructure contains a large number of intergranular and isolated cementite carbides inherited form the hot-rolling stage and distributed outside the pearlite islands. These carbides contain about one third of the carbon of the steel. The pearlitic cementite contains the remainder of the carbon.
- These isolated carbides play a predominant role in the austenite morphogenesis. A necklace or a banded austenite microstructure is generated respectively on slow and fast heating, depending on whether or not the ferrite recrystallization has enough time to modify their spatial distribution with respect to the ferrite grain boundaries, and thus the nucleation sites and the carbon sources for the austenite. Our experimental results sustain the analysis proposed by Li et al. [26].
- The austenite transformation starts with a slow kinetic regime corresponding to the cementite dissolution involving the partition of the substitutional elements.
- Two sub-systems with different kinetic behavior are then identified. The pearlite islands transform simultaneously to austenite in a narrow temperature range which depends weakly on the heating rate. The process still involves the partition of the substitutional elements, but is accelerated because of the low diffusion distances inside the pearlitic ferrite. In contrast, the austenite nucleates and grows more progressively from the isolated carbides. The latter dissolve quickly, without partition, once some critical partition-non

partition transition temperature (PNTT) has been reached. The PNTT is predictable from thermodynamic data; it increases with increasing Mn concentration in cementite carbides.

- During heating up to 800°C, the final stage corresponds to a ferrite to austenite transformation, without partition of the substitutional elements. During the isothermal holding at 800°C, the austenite transformation continues with partition. The rate-limiting process is the diffusion of substitutional elements in the ferrite and finally in the austenite.
- The faster transformation during faster heating is largely explained by the partitionless austenite transformation during this last stage, as shown by DICTRA simulations. The austenite fraction stays close to a maximum value which only depends on the temperature and which is predictable from thermodynamics (NPLE fraction). However, other possible origins such as the presence of non-recrystallized ferrite or faster nucleation should still be considered.
- DICTRA simulations of austenite transformation achieve to predict kinetics orders of magnitude during the heating stage and the influence of the heating rate. However, the geometrical representation of the microstructure has to be improved for accurate predictions and to encompass both the heating and the holding stages in the simulations.

6 Acknowledgements

This research was funded by the Centre National de la Recherche Scientifique (CNRS) and by ArcelorMittal Maizières-lès-Metz (Product Research Centre). The Laboratory of Excellence on Design of Alloy Metals for low-mAss Structures (Labex DAMAS belongs to the program "Investment in the future" operated by the National Research Agency (ANR) and referenced by ANR-11-LABX-0008-01) from Université de Lorraine (France) is also fully acknowledged for its support. Dr M. Salib and Mr G. Petitgand (at ArcelorMittal) are

1097 acknowledged for the EBSD observation and the WDS analyses. Dr J. Ghanbaja (IJL) is
1098 acknowledged for the TEM observations and EDS analyses.

1099

1100 **7 Bibliography**

1101 [1] G.R. Speich, V.A. Demarest, R.L. Miller, Formation of Austenite During Intercritical
1102 Annealing of Dual-Phase Steels, Metall. Mater. Trans. A. 12 (1981) 1419–1428.
1103 https://doi.org/10.1007/BF02643686.

1104 [2] M. Kulakov, W.J. Poole, M. Militzer, The Effect of the Initial Microstructure on
1105 Recrystallization and Austenite Formation in a DP600 Steel, Metall. Mater. Trans. A. 44
1106 (2013) 3564–3576. https://doi.org/10.1007/s11661-013-1721-z.

1107 [3] T. Allam, M. Abbas, Mechanical Properties, Formability, and Corrosion Behavior of
1108 Dual Phase Weathering Steels Developed by an Inter-Critical Annealing Treatment, Steel
1109 Res. Int. 86 (2015) 231–240. https://doi.org/10.1002/srin.201400033.

1110 [4] H. Hofmann, D. Mattissen, T.W. Schaumann, Advanced cold rolled steels for
1111 automotive applications, Mater. Werkst. 37 (2006) 716–723.
1112 https://doi.org/10.1002/mawe.200600057.

1113 [5] E. De Moor, D.K. Matlock, J.G. Speer, M.J. Merwin, Austenite stabilization through
1114 manganese enrichment, Scr. Mater. 64 (2011) 185–188.
1115 https://doi.org/10.1016/j.scriptamat.2010.09.040.

1116 [6] P. Movahed, S. Kolahgar, S.P.H. Marashi, M. Pouranvari, N. Parvin, The effect of
1117 intercritical heat treatment temperature on the tensile properties and work hardening behavior
1118 of ferrite–martensite dual phase steel sheets, Mater. Sci. Eng. A. 518 (2009) 1–6.
1119 https://doi.org/10.1016/j.msea.2009.05.046.

[7] S.Y.P. Allain, I. Pushkareva, J. Teixeira, M. Gouné, C. Scott, Dual-Phase Steels: The First Family of Advanced High Strength Steels, in: Ref. Module Mater. Sci. Mater. Eng., Elsevier, 2020. https://doi.org/10.1016/B978-0-12-819726-4.00057-0.

[8] N. Fonstein, Advanced High Strength Sheet Steels Physical Metallurgy, Design, Processing, and Properties, Springer, Cham, n.d. https://doi.org/10.1007/978-3-319-19165-2.

[9] M. Erdogan, Effect of austenite dispersion on phase transformation in dual phase steel, Scr. Mater. 48 (2003) 501–506. https://doi.org/10.1016/S1359-6462(02)00500-6.

[10] P. Jacques, F. Delannay, X. Cornet, Ph. Harlet, J. Ladriere, Enhancement of the mechanical properties of a low-carbon, low-silicon steel by formation of a multiphased microstructure containing retained Austenite, Metall. Mater. Trans. A. 29 (1998) 2383–2393. https://doi.org/10.1007/s11661-998-0114-1.

[11] S.Y.P. Allain, O. Bouaziz, I. Pushkareva, C.P. Scott, Towards the microstructure design of DP steels: A generic size-sensitive mean-field mechanical model, Mater. Sci. Eng. A. 637 (2015) 222–234. https://doi.org/10.1016/j.msea.2015.04.017.

[12] C.C. Tasan, J.P.M.M. Hoefnagels, M. Diehl, D. Yan, F. Roters, D. Raabe, Strain localization and damage in dual phase steels investigated by coupled in-situ deformation experiments and crystal plasticity simulations, Int. J. Plast. 63 (2014) 198–210. https://doi.org/10.1016/j.ijplas.2014.06.004.

[13] G. Avramovic-Cingara, Y. Ososkov, M.K. Jain, D.S. Wilkinson, Effect of martensite distribution on damage behaviour in {DP600} dual phase steels, Mater. Sci. Eng. A. 516 (2009) 7–16. https://doi.org/10.1016/j.msea.2009.03.055.

[14] V. Uthaisangsuk, S. Muenstermann, U. Prahl, W. Bleck, H.-P. Schmitz, T. Pretorius, A study of microcrack formation in multiphase steel using representative volume element and damage mechanics, Comput. Mater. Sci. 50 (2011) 1225–1232.

1144 https://doi.org/10.1016/j.commatsci.2010.08.007.

1145 [15] K. Ismail, A. Perlade, P.J. Jacques, T. Pardoen, L. Brassart, Impact of second phase
1146 morphology and orientation on the plastic behavior of dual-phase steels, Int. J. Plast. 118
1147 (2019) 130–146. https://doi.org/10.1016/j.ijplas.2019.02.005.

1148 [16] S.D. Martín, de T. Cock, A. García-Junceda, F.G. Caballero, C. Capdevila, C.G. de
1149 Andrés, Effect of heating rate on reaustenitisation of low carbon niobium microalloyed steel,
1150 Mater. Sci. Technol. 24 (2008) 266–272. https://doi.org/10.1179/174328408X265640.

1151 [17] J. Agren, H. Abe, T. Suzuki, Y. Sakuma, The dissolution of cementite in a low carbon
1152 steel during isothermal annealing at 700°C, Metall. Trans. A. 17 (1986) 617–620.
1153 https://doi.org/10.1007/BF02643980.

1154 [18] A. Arlazarov, M. Gouné, O. Bouaziz, A. Hazotte, G. Petitgand, P. Barges, Evolution
1155 of microstructure and mechanical properties of medium Mn steels during double annealing,
1156 Mater. Sci. Eng. A. 542 (2012) 31–39. https://doi.org/10.1016/j.msea.2012.02.024.

1157 [19] M. Mazinani, W.J. Poole, Effect of Martensite Plasticity on the Deformation Behavior
1158 of a Low-Carbon Dual-Phase Steel, Metall. Mater. Trans. A. 38 (2007) 328–339.
1159 https://doi.org/10.1007/s11661-006-9023-3.

1160 [20] G. Avramovic-Cingara, Y. Ososkov, M.K. Jain, D.S. Wilkinson, Effect of martensite
1161 distribution on damage behaviour in DP600 dual phase steels, Mater. Sci. Eng. A. 516 (2009)
1162 7–16. https://doi.org/10.1016/j.msea.2009.03.055.

1163 [21] C.C. Tasan, J.P.M. Hoefnagels, M. Diehl, D. Yan, F. Roters, D. Raabe, Strain
1164 localization and damage in dual phase steels investigated by coupled in-situ deformation
1165 experiments and crystal plasticity simulations, Int. J. Plast. 63 (2014) 198–210.
1166 https://doi.org/10.1016/j.ijplas.2014.06.004.

1167 [22] V. Andrade-Carozzo, P.J. Jacques, Interactions between Recrystallisation and Phase

1168 Transformations during Annealing of Cold Rolled Nb-Added TRIP-Aided Steels, Mater. Sci.
1169 Forum. 539–543 (2007) 4649–4654. https://doi.org/10.4028/www.scientific.net/MSF.539-
1170 543.4649.

1171 [23] H. Azizi-Alizamini, M. Militzer, W.J. Poole, Austenite Formation in Plain Low-
1172 Carbon Steels, Metall. Mater. Trans. A. 42 (2011) 1544–1557.
1173 https://doi.org/10.1007/s11661-010-0551-5.

1174 [24] A. Chbihi, D. Barbier, L. Germain, A. Hazotte, M. Gouné, Interactions between ferrite
1175 recrystallization and austenite formation in high-strength steels, J. Mater. Sci. 49 (2014)
1176 3608–3621. https://doi.org/10.1007/s10853-014-8029-2.

1177 [25] J. Huang, W.J. Poole, M. Militzer, Austenite formation during intercritical annealing,
1178 Metall. Mater. Trans. A. 35 (2004) 3363–3375. https://doi.org/10.1007/s11661-004-0173-x.

1179 [26] P. Li, J. Li, Q. Meng, W. Hu, D. Xu, Effect of heating rate on ferrite recrystallization
1180 and austenite formation of cold-roll dual phase steel, J. Alloys Compd. 578 (2013) 320–327.
1181 https://doi.org/10.1016/j.jallcom.2013.05.226.

1182 [27] L.S. Thomas, D.K. Matlock, Formation of Banded Microstructures with Rapid
1183 Intercritical Annealing of Cold-Rolled Sheet Steel, Metall. Mater. Trans. A. 49 (2018) 4456–
1184 4473. https://doi.org/10.1007/s11661-018-4742-9.

1185 [28] R.R. Mohanty, O.A. Girina, N.M. Fonstein, Effect of Heating Rate on the Austenite
1186 Formation in Low-Carbon High-Strength Steels Annealed in the Intercritical Region, Metall.
1187 Mater. Trans. A. 42 (2011) 3680–3690. https://doi.org/10.1007/s11661-011-0753-5.

1188 [29] D. Barbier, L. Germain, A. Hazotte, M. Gouné, A. Chbihi, Microstructures resulting
1189 from the interaction between ferrite recrystallization and austenite formation in dual-phase
1190 steels, J. Mater. Sci. 50 (2015) 374–381. https://doi.org/10.1007/s10853-014-8596-2.

1191 [30] Q. Lai, M. Gouné, A. Perlade, T. Pardoen, P. Jacques, O. Bouaziz, Y. Bréchet,

1192 Mechanism of Austenite Formation from Spheroidized Microstructure in an Intermediate Fe-
1193 0.1C-3.5Mn Steel, Metall. Mater. Trans. A. 47 (2016) 3375–3386.
1194 https://doi.org/10.1007/s11661-016-3547-y.

1195 [31] R. Wei, M. Enomoto, R. Hadian, H.S. Zurob, G.R. Purdy, Growth of austenite from
1196 as-quenched martensite during intercritical annealing in an Fe–0.1C–3Mn–1.5Si alloy, Acta
1197 Mater. (2013) 11.

1198 [32] C.I. Garcia, A.J. Deardo, Formation of austenite in 1.5 pct Mn steels, Metall. Trans. A.
1199 12 (1981) 521–530. https://doi.org/10.1007/BF02648551.

1200 [33] D.Z. Yang, E.L. Brown, D.K. Matlock, G. Krauss, Ferrite recrystallization and
1201 austenite formation in cold-rolled intercritically annealed steel, Metall. Trans. A. 16 (1985)
1202 1385–1392. https://doi.org/10.1007/BF02658671.

1203 [34] S. Chattopadhyay, C.M. Sellars, Quantitative measurements of pearlite
1204 spheroidization, Metallography. 10 (1977) 89–105. https://doi.org/10.1016/0026-
1205 0800(77)90044-1.

1206 [35] S. Chattopadhyay, C.M. Sellars, Kinetics of pearlite spheroidisation during static
1207 annealing and during hot deformation, Acta Metall. 30 (1982) 157–170.
1208 https://doi.org/10.1016/0001-6160(82)90055-4.

1209 [36] M. Etou, S. Fukushima, T. Sasaki, Y. Haraguchi, K. Miyata, M. Wakita, T. Tomida,
1210 N. Imai, M. Yoshida, Y. Okada, Super Short Interval Multi-pass Rolling Process for
1211 Ultrafine-grained Hot Strip, ISIJ Int. 48 (2008) 1142–1147.
1212 https://doi.org/10.2355/isijinternational.48.1142.

1213 [37] Y. Yin, J. Sun, A. Zhao, J. Gou, Ultra-low-carbon steel spheroidization and torsion, J.
1214 Iron Steel Res. Int. 25 (2018) 968–974. https://doi.org/10.1007/s42243-018-0137-9.

1215 [38] T.H. Courtney, J.C.M. Kampe, Shape instabilities of plate-like structures—II.

1216 Analysis, Acta Metall. 37 (1989) 1747–1758. https://doi.org/10.1016/0001-6160(89)90060-6.

1217 [39] J. Arruabarrena, B. López, J.M. Rodriguez-Ibabe, Influence of Prior Warm
1218 Deformation on Cementite Spheroidization Process in a Low-Alloy Medium Carbon Steel,
1219 Metall. Mater. Trans. A. 45 (2014) 1470–1484. https://doi.org/10.1007/s11661-013-2066-3.

1220 [40] J.J. Yi, I.S. Kim, H.S. Choi, Austenitization during intercritical annealing of an Fe-C-
1221 Si-Mn dual-phase steel, Metall. Trans. A. 16 (1985) 1237–1245.
1222 https://doi.org/10.1007/BF02670328.

1223 [41] Z.-K. Liu, L. Höglund, B. Jönsson, J. ågren, An experimental and theoretical study of
1224 cementite dissolution in an Fe-Cr-C alloy, Metall. Trans. A. 22 (1991) 1745–1752.
1225 https://doi.org/10.1007/BF02646498.

1226 [42] G. Miyamoto, H. Usuki, Effects of Mn, Si and Cr addition on reverse transformation
1227 at 1073K from spheroidized cementite structure in Fe–0.6 mass% C alloy, Acta Mater. (2010)
1228 11.

1229 [43] M. Gouné, P. Maugis, J. Drillet, A Criterion for the Change from Fast to Slow Regime
1230 of Cementite Dissolution in Fe–C–Mn Steels, J. Mater. Sci. Technol. 28 (2012) 728–736.
1231 https://doi.org/10.1016/S1005-0302(12)60122-4.

1232 [44] Y. Xia, M. Enomoto, Z. Yang, Z. Li, C. Zhang, Effects of alloying elements on the
1233 kinetics of austenitization from pearlite in Fe–C–M alloys, Philos. Mag. 93 (2013) 1095–
1234 1109. https://doi.org/10.1080/14786435.2012.744484.

1235 [45] M. Enomoto, S. Li, Z.N. Yang, C. Zhang, Z.G. Yang, Partition and non-partition
1236 transition of austenite growth from a ferrite and cementite mixture in hypo- and
1237 hypereutectoid Fe-C-Mn alloys, Calphad. 61 (2018) 116–125.
1238 https://doi.org/10.1016/j.calphad.2018.03.002.

1239 [46] M. HILLERT, K. NILSSON, L. TORNDAHL, EFFECT OF ALLOYING

ELEMENTS ON FORMATION OF AUSTENITE AND DISSOLUTION OF CEMENTITE, J. Iron Steel Inst. 209 (1971) 49-.

[47] Y.X. Wu, L.Y. Wang, W.W. Sun, M.J. Styles, A.J. Studer, Y. Bréchet, A. Arlazarov, C.R. Hutchinson, Austenite formation kinetics from multicomponent cementite-ferrite aggregates, Acta Mater. 196 (2020) 470–487. https://doi.org/10.1016/j.actamat.2020.07.001.

[48] A. Marceaux dit Clément, K. Hoummada, J. Drillet, V. Hébert, P. Maugis, Effects of cementite size and chemistry on the kinetics of austenite formation during heating of a high-formability steel, Comput. Mater. Sci. 182 (2020) 109786. https://doi.org/10.1016/j.commatsci.2020.109786.

[49] M. Moreno, J. Teixeira, J. Ghanbaja, F. Bonnet, S. Allain, Evolution of cementite composition along the processing of cold-rolled and annealed Dual-Phase steels, Materialia. 6 (2019) 100179. https://doi.org/10.1016/j.mtla.2018.100179.

[50] R. Petrov, L. Kestens, Y. Houbaert, Recrystallization of a Cold Rolled Trip-assisted Steel during Reheating for Intercritical Annealling., ISIJ Int. 41 (2001) 883–890. https://doi.org/10.2355/isijinternational.41.883.

[51] N. Maruyama, T. Ogawa, M. Takahashi, Recrystallisation at Intercritical Annealing in Low Carbon Steels, Mater. Sci. Forum. (2007). https://doi.org/10.4028/www.scientific.net/MSF.558-559.247.

[52] S. Dillien, M. Seefeldt, S. Allain, O. Bouaziz, P. Van Houtte, EBSD study of the substructure development with cold deformation of dual phase steel, Mater. Sci. Eng. A. 527 (2010) 947–953. https://doi.org/10.1016/j.msea.2009.09.009.

[53] M. Ollat, Characterization and modeling of microstructural evolutions during the thermal treatment of cold-rolled Dual-Phase steels, phdthesis, Université de Lyon, 2017. https://tel.archives-ouvertes.fr/tel-01920855 (accessed January 30, 2020).

1264 [54] T. Ogawa, N. Maruyama, N. Sugiura, N. Yoshinaga, Incomplete Recrystallization and
1265 Subsequent Microstructural Evolution during Intercritical Annealing in Cold-rolled Low
1266 Carbon Steels, ISIJ Int. 50 (2010) 7.

1267 [55] M. Moreno, J. Teixeira, G. Geandier, J.-C. Hell, F. Bonnet, M. Salib, S. Allain, Real-
1268 Time Investigation of Recovery, Recrystallization and Austenite Transformation during
1269 Annealing of a Cold-Rolled Steel Using High Energy X-ray Diffraction (HEXRD), Metals. 9
1270 (2018) 8. https://doi.org/10.3390/met9010008.

1271 [56] Bouaziz O, Le Corre C, Flow stress and microstructure modelling of ferrite-pearlite
1272 steels during cold rolling, Mater. Sci. Forum. 426–4 (2003) 1399–1404.
1273 https://www.cheric.org/research/tech/periodicals/view.php?seq=1254580.

1274 [57] S. Allain, O. Bouaziz, Microstructure based modeling for the mechanical behavior of
1275 ferrite–pearlite steels suitable to capture isotropic and kinematic hardening, Mater. Sci. Eng.
1276 A. 496 (2008) 329–336. https://doi.org/10.1016/j.msea.2008.06.009.

1277 [58] ASTM E112-96e2. Standard Test Methods for Determining Average Grain Size,
1278 ASTM International, West Conshohocken, PA, 1996. https://doi.org/10.1520/E0112-96E02.

1279 [59] ASTM E562-08. Test Method for Determining Volume Fraction by Systematic
1280 Manual Point Count, ASTM International, West Conshohocken, PA, 2008.
1281 https://doi.org/10.1520/E0562-08.

1282 [60] K. Radwański, Application of FEG-SEM and EBSD Methods for the Analysis of the
1283 Restoration Processes Occurring During Continuous Annealing of Dual-Phase Steel Strips,
1284 Steel Res. Int. 86 (2015) 1379–1390. https://doi.org/10.1002/srin.201400361.

1285 [61] M. Moreno, Mécanismes métallurgiques et leurs interactions au recuit d'aciers ferrito-
1286 perlitiques laminés : caractérisation et modélisation, Université de Lorraine, 2019.

1287 [62] S.A. Saltikov, The Determination of the Size Distribution of Particles in an Opaque

1288 Material from a Measurement of the Size Distribution of Their Sections, in: H. Elias (Ed.),
1289 Stereology, Springer, Berlin, Heidelberg, 1967: pp. 163–173. https://doi.org/10.1007/978-3-
1290 642-88260-9_31.

1291 [63] J.C. Russ, Practical Stereology, Springer US, 1986. https://doi.org/10.1007/978-1-
1292 4899-3533-5.

1293 [64] S.Y.P. Allain, S. Gaudez, G. Geandier, J.-C. Hell, M. Gouné, F. Danoix, M. Soler, S.
1294 Aoued, A. Poulon-Quintin, Internal stresses and carbon enrichment in austenite of Quenching
1295 and Partitioning steels from high energy X-ray diffraction experiments, Mater. Sci. Eng. A.
1296 710 (2018) 245–250. https://doi.org/10.1016/j.msea.2017.10.105.

1297 [65] A.P. Hammersley, S.O. Svensson, M. Hanfland, A.N. Fitch, D. Hausermann, Two-
1298 dimensional detector software: From real detector to idealised image or two-theta scan, High
1299 Press. Res. 14 (1996) 235–248. https://doi.org/10.1080/08957959608201408.

1300 [66] THE FIT2D HOME PAGE, (n.d.). http://www.esrf.eu/computing/scientific/FIT2D/
1301 (accessed January 20, 2020).

1302 [67] H.M. Rietveld, Line profiles of neutron powder-diffraction peaks for structure
1303 refinement, Acta Crystallogr. 22 (1967) 151–152.
1304 https://doi.org/10.1107/S0365110X67000234.

1305 [68] J. Rodríguez-Carvajal, Recent advances in magnetic structure determination by
1306 neutron powder diffraction, Phys. B Condens. Matter. 192 (1993) 55–69.
1307 https://doi.org/10.1016/0921-4526(93)90108-I.

1308 [69] J.-W. Lee, P.R. Howell, Microstructural development in non-oriented lamination
1309 steels, J. Mater. Sci. 22 (1987) 3631–3641. https://doi.org/10.1007/BF01161471.

1310 [70] J.-W. Lee, S.W. Thompson, P.R. Howell, Microstructural development in non-
1311 oriented lamination steels, J. Mater. Sci. 25 (1990) 1699–1710.

https://doi.org/10.1007/BF01045373.

[71] J.W. Lee, S.W. Thompson, R. Varughese, P.R. Howell, The interaction between proeutectoid ferrite and austenite during the isothermal transformation of two low-carbon steels — a new model for the decomposition of austenite, J. Mater. Sci. 28 (1993) 4571–4577. https://doi.org/10.1007/BF00414244.

[72] Y. Granbom, L. Ryde, J. Jeppsson, Simulation of the Soaking and Gas Jet Cooling in a Continuous Annealing Line using Dilatometry, Steel Res. Int. 81 (2010) 158–167. https://doi.org/10.1002/srin.200900097.

[73] M. Ollat, V. Massardier, D. Fabregue, E. Buscarlet, F. Keovilay, M. Perez, Modeling of the Recrystallization and Austenite Formation Overlapping in Cold-Rolled Dual-Phase Steels During Intercritical Treatments, Metall. Mater. Trans. A. 48 (2017) 4486–4499. https://doi.org/10.1007/s11661-017-4231-6.

[74] S.Y.P. Allain, M. Moreno, M. Lamari, H. Zurob, J. Teixeira, F. Bonnet, A Physics-Based Mean-Field Model for Ferrite Recovery and Recrystallization, Metals. 10 (2020) 622. https://doi.org/10.3390/met10050622.

[75] V.I. Savran, Y. Van Leeuwen, D.N. Hanlon, C. Kwakernaak, W.G. Sloof, J. Sietsma, Microstructural Features of Austenite Formation in C35 and C45 alloys, Metall. Mater. Trans. A. 38 (2007) 946–955. https://doi.org/10.1007/s11661-007-9128-3.

[76] V.I. Savran, S.E. Offerman, J. Sietsma, Austenite Nucleation and Growth Observed on the Level of Individual Grains by Three-Dimensional X-Ray Diffraction Microscopy, Metall. Mater. Trans. A. 41 (2010) 583–591. https://doi.org/10.1007/s11661-009-0142-5.

[77] S.E. Offerman, N.H. van Dijk, J. Sietsma, S. Grigull, E.M. Lauridsen, L. Margulies, H.F. Poulsen, M.T. Rekveldt, S. van der Zwaag, Grain Nucleation and Growth During Phase Transformations, Science. 298 (2002) 1003–1005. https://doi.org/10.1126/science.1076681.

[78] J.-O. Andersson, T. Helander, L. Höglund, P. Shi, B. Sundman, Thermo-Calc & DICTRA, computational tools for materials science, Calphad. 26 (2002) 273–312. https://doi.org/10.1016/S0364-5916(02)00037-8.

[79] M.G. Mecozzi, C. Bos, J. Sietsma, A mixed-mode model for the ferrite-to-austenite transformation in a ferrite/pearlite microstructure, Acta Mater. 88 (2015) 302–313. https://doi.org/10.1016/j.actamat.2015.01.058.

[80] M. Ollat, M. Militzer, V. Massardier, D. Fabregue, E. Buscarlet, F. Keovilay, M. Perez, Mixed-mode model for ferrite-to-austenite phase transformation in dual-phase steel, Comput. Mater. Sci. (2018) 9.

[81] B. Zhu, M. Militzer, Phase-Field Modeling for Intercritical Annealing of a Dual-Phase Steel, Metall. Mater. Trans. A. 46 (2015) 1073–1084. https://doi.org/10.1007/s11661-014-2698-y.

[82] F. Huyan, J.-Y. Yan, L. Höglund, J. Ågren, A. Borgenstam, Simulation of the Growth of Austenite from As-Quenched Martensite in Medium Mn Steels, Metall. Mater. Trans. A. 49 (2018) 1053–1060. https://doi.org/10.1007/s11661-018-4497-3.

[83] A. Roósz, Z. Gácsi, E.G. Fuchs, Isothermal formation of austenite in eutectoid plain carbon steel, Acta Metall. 31 (1983) 509–517. https://doi.org/10.1016/0001-6160(83)90039-1.

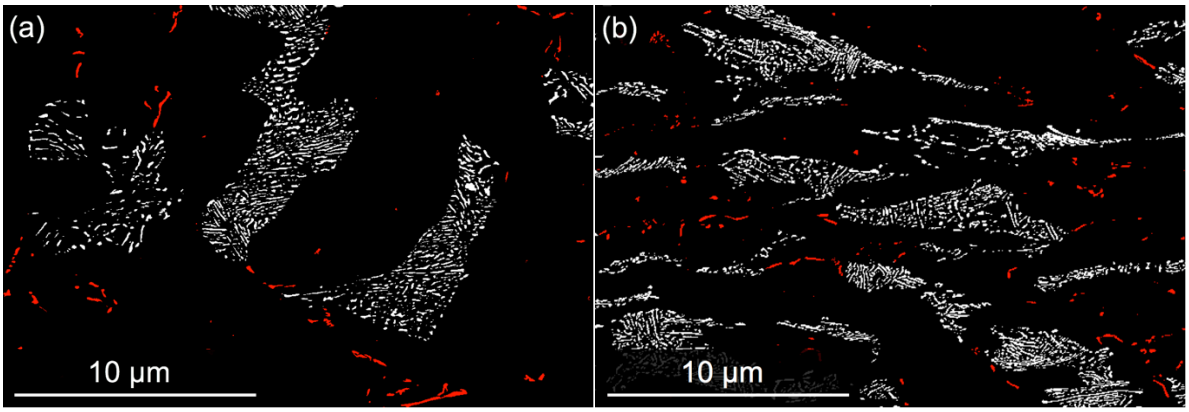

Figure 17. SEM micrographs treated by image analysis representative of the hot-rolled (a) and cold-rolled (b) microstructures. The ferrite is represented in black, the pearlitic cementite in white and the isolated carbides in red.

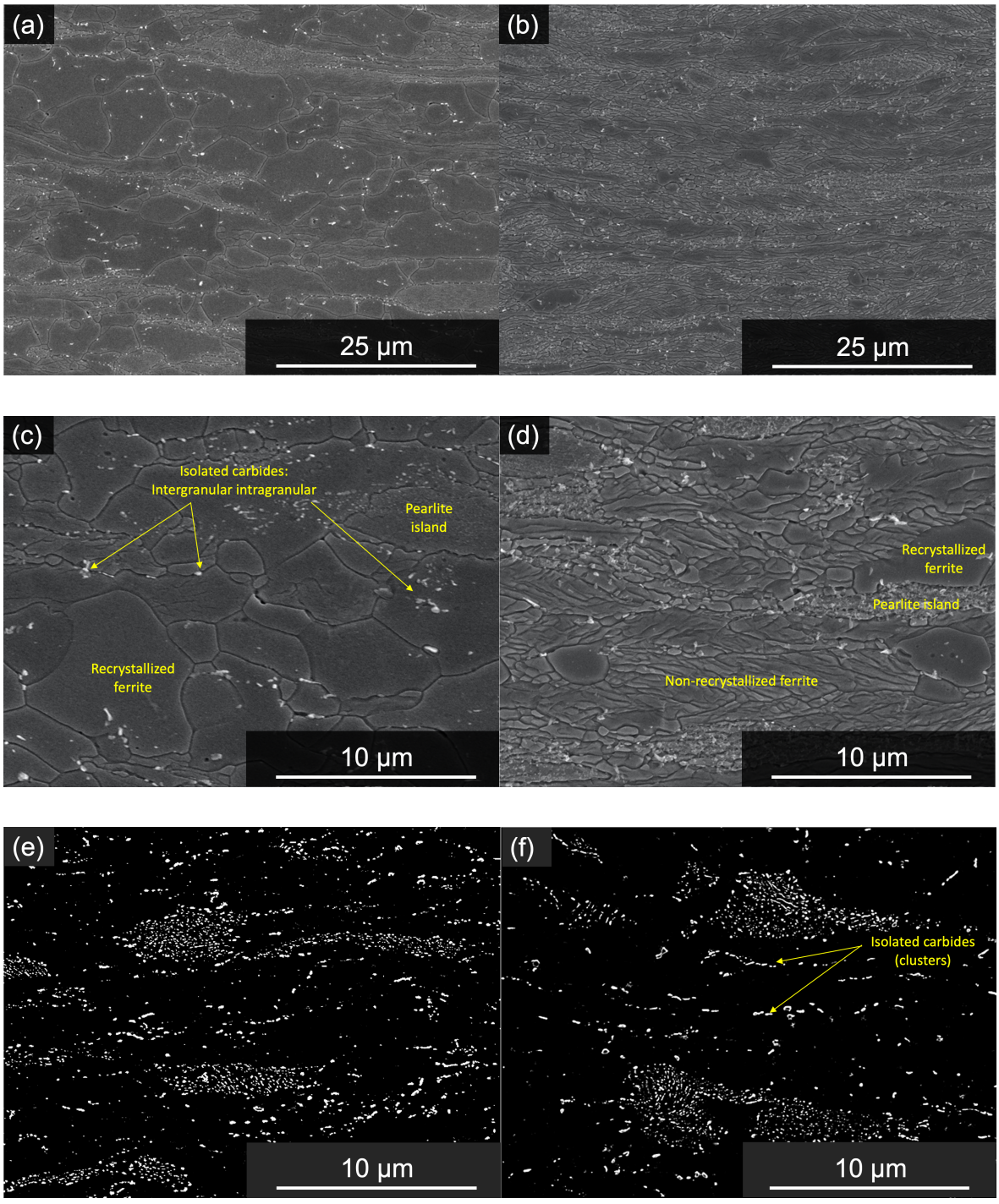

Figure 18. SEM micrographs representative of the microstructure after heating to a,c,e) 700°C at 3°C.s^{-1}; b,d, f) 720°C at 30°C.s^{-1}. Figures c and d correspond to views at higher magnification of a and b. Figures e and f have been threshold to reveal carbide microstructures in both cases (carbides in bright contrast).

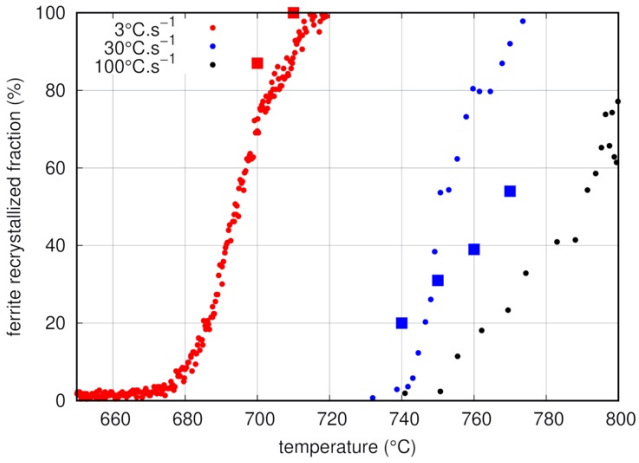

Figure 19. Fraction of recrystallized ferrite as a function of the temperature during heating at 3, 30 or 100°C.s^{-1}. Dots: HEXRD, squares: SEM at 30°C.s^{-1} or EBSD at 3°C.s^{-1}. (In the SEM analyses, the pearlitic ferrite was excluded).

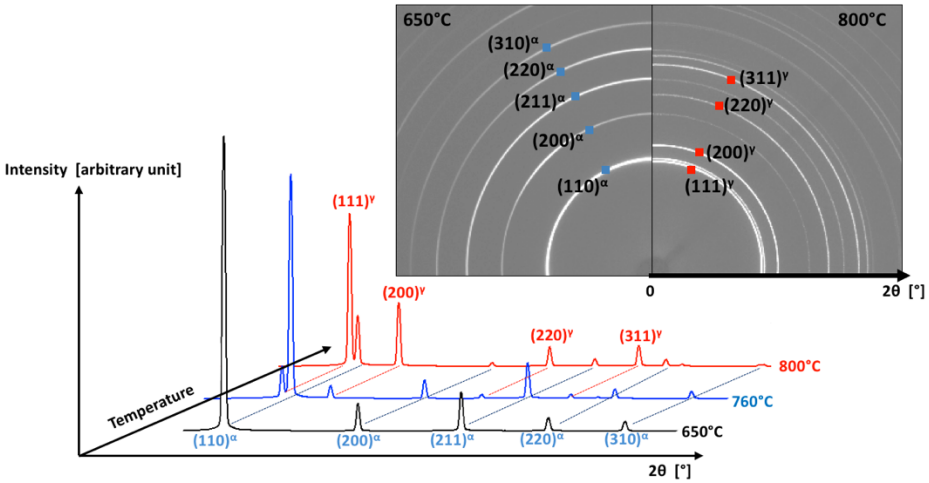

Figure 20. 2D Debye-Scherrer rings recorded at 650 and 800°C during heating at 3°C.s^{-1}. Intensity-2θ profiles from circular integration of the DS rings at 650, 760 and 800°C.

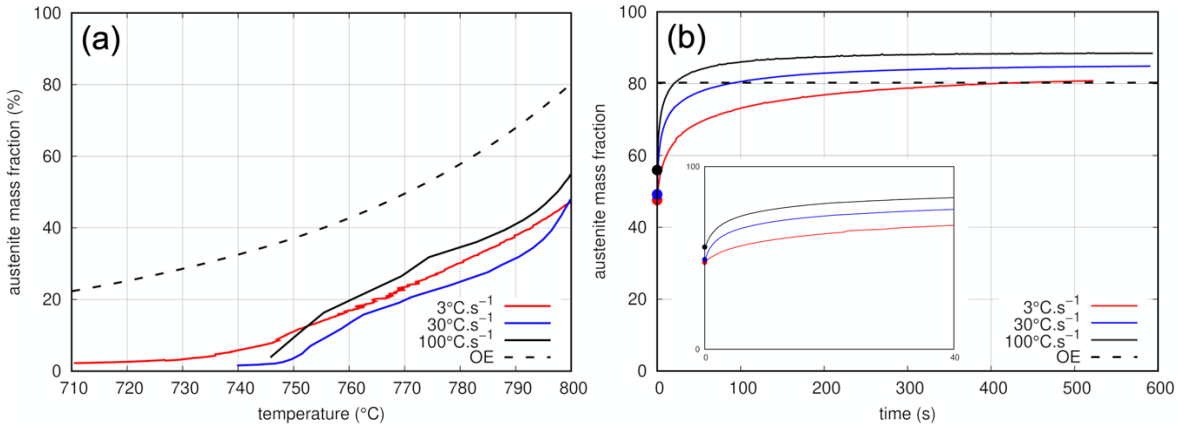

Figure 21. Austenite mass fraction as a function of a) temperature during heating; b) time during isothermal annealing at 800°C (zoom on first stages in the insert). Time scale starts at the beginning of the isothermal annealing in b). The dots indicate the austenite fraction at the start of the isothermal annealing.

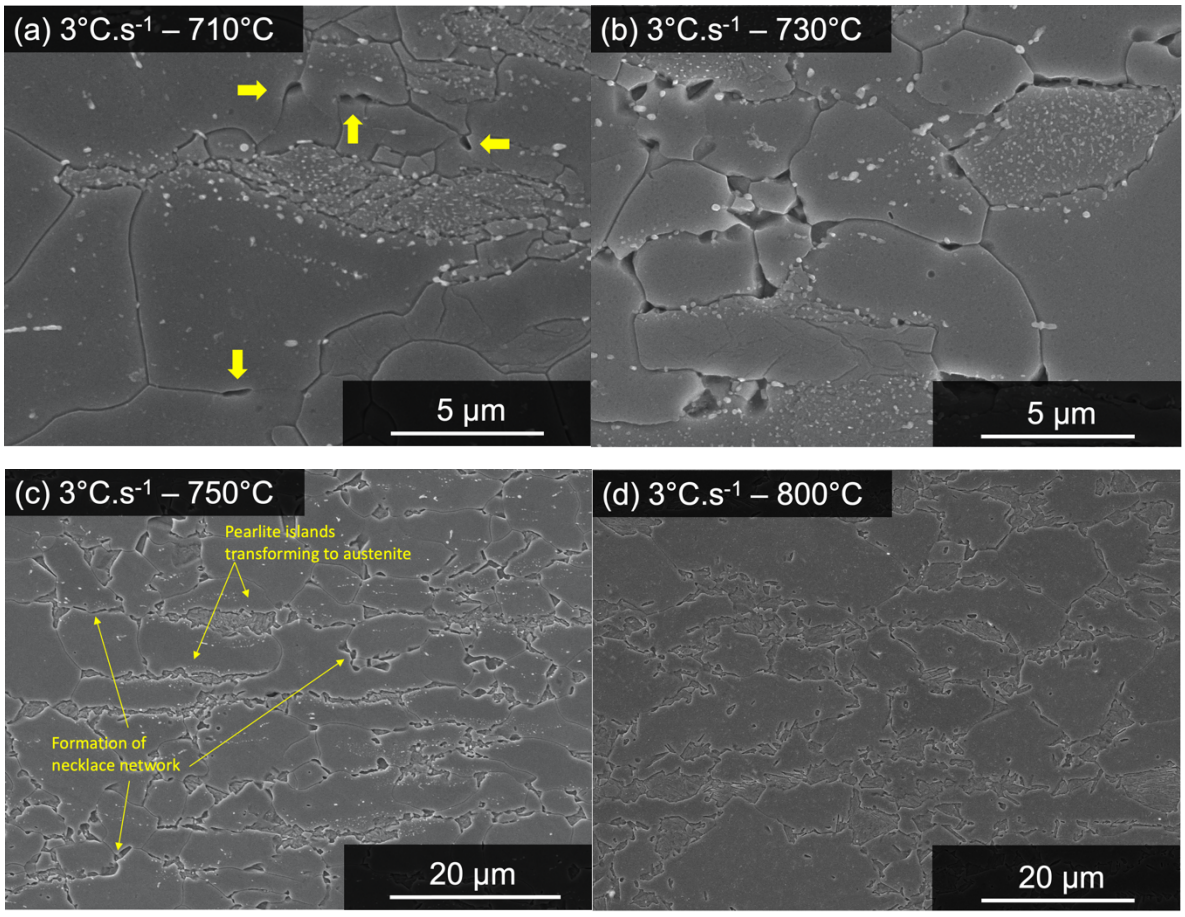

Figure 22. SEM observations (Dino etching) of the microstructure after heating at 3°C.s^{-1} followed by quench up to a) 710°C; b) 730°C; c) 750°C; d) 800°C. In a), the arrows show the first grains of austenite.

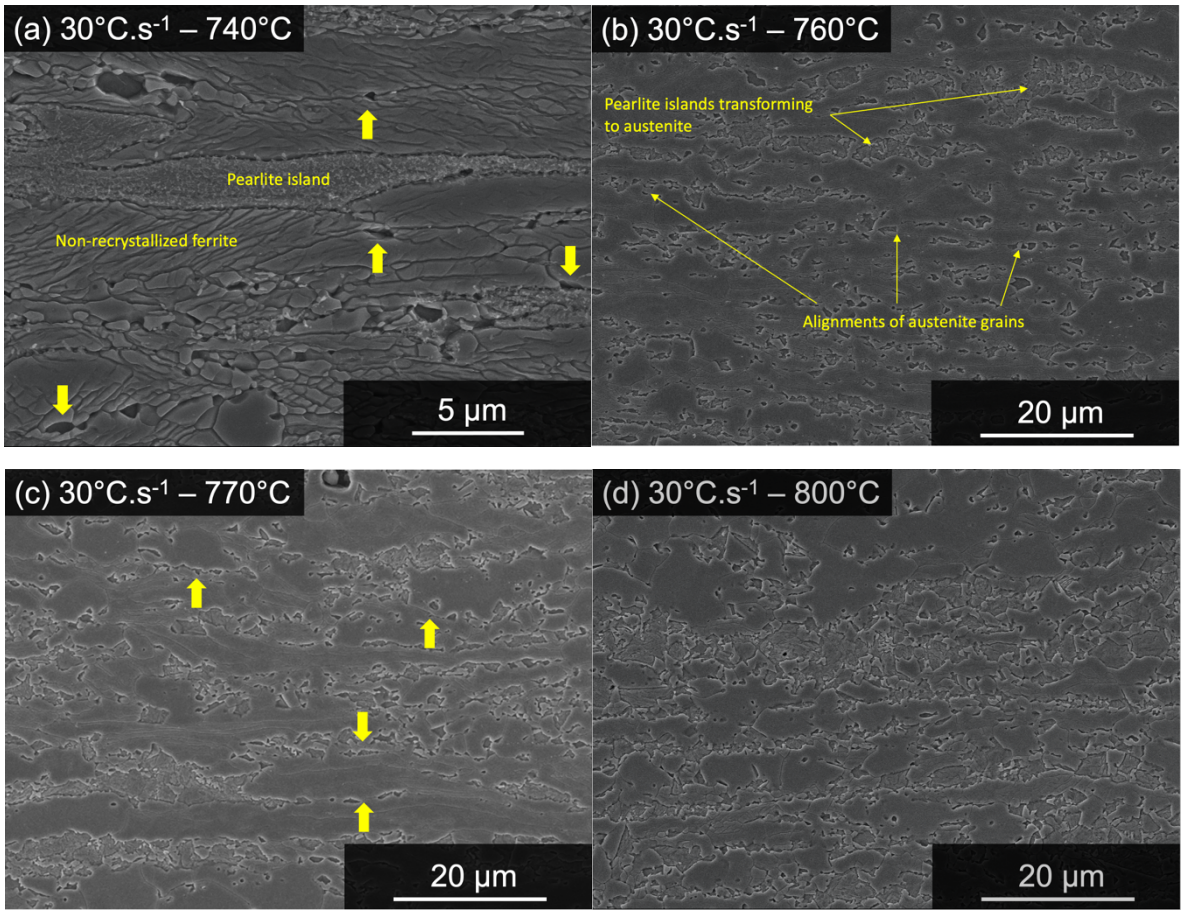

Figure 23. SEM observations (Dino etching) of the microstructure after heating at 30°C.s^{-1} followed by quench up to a) 740°C; b) 760°C; c) 770°C; d) 800°C. The arrows indicate: first austenite grains in (a); alignments of austenite grains at the boundaries of elongated recrystallized ferrite grains in (c).

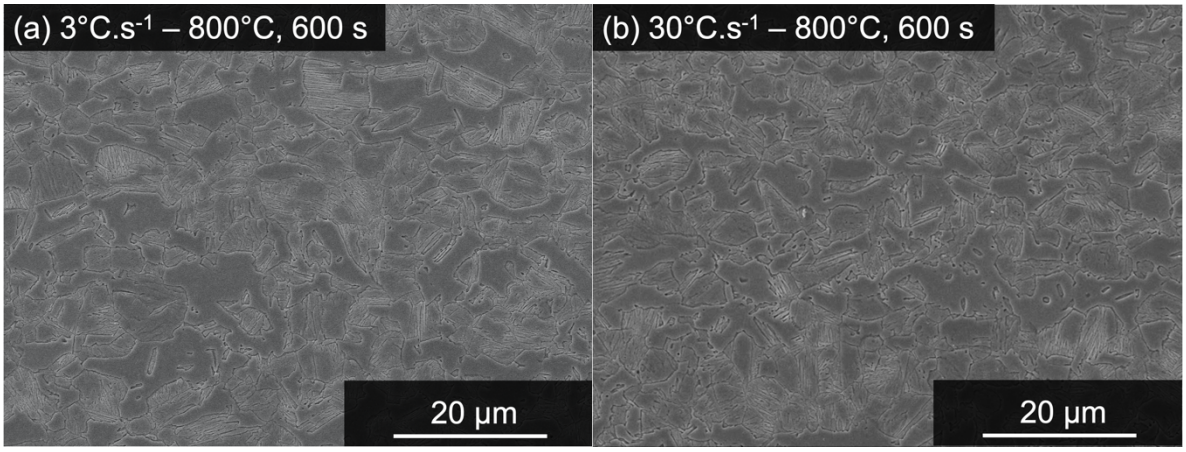

Figure 24. SEM observations (Dino etching) of the microstructure after heating up to 800°C and isothermal annealing for 600 s. a) 3°C.s^{-1}; b) 30°C.s^{-1}.

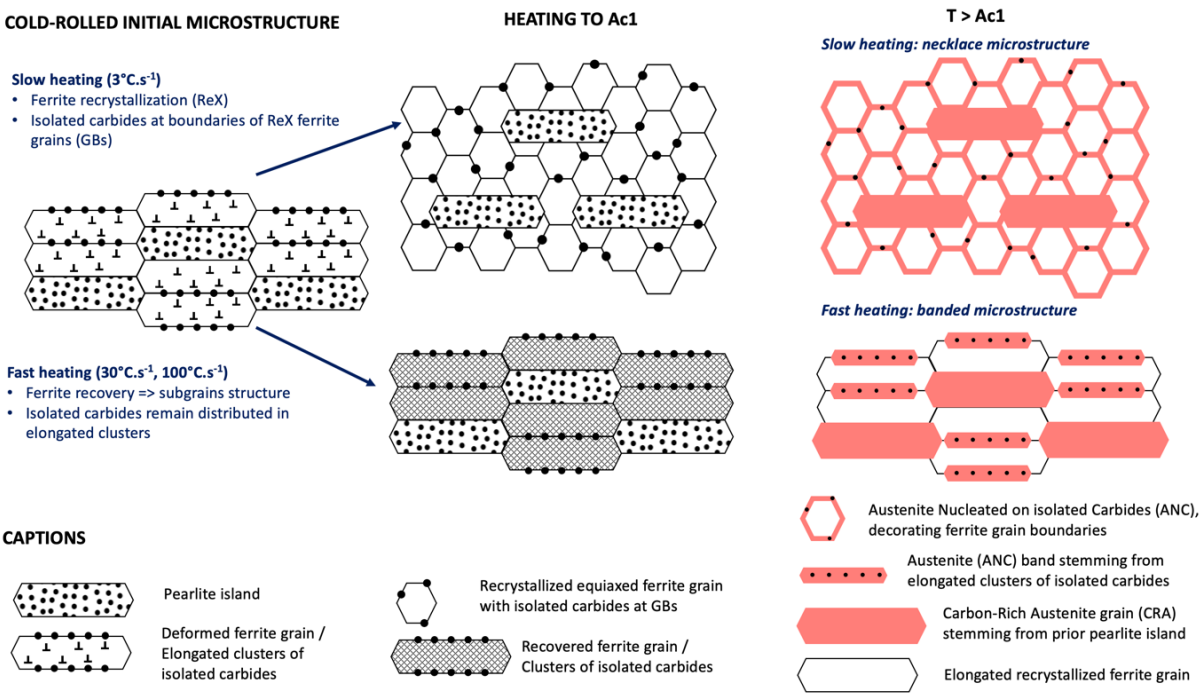

Figure 25. Schematic of the austenite morphogenesis depending on the heating rate.

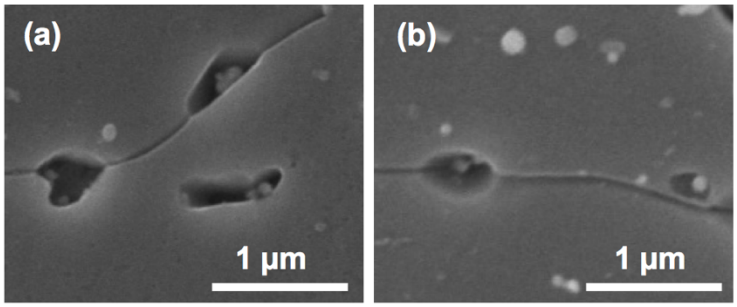

Figure 26. SEM micrographs (Dino etchant) showing austenite grains nucleated on ferrite grain boundaries after heating to 730°C at 3°C.s^{-1}. Cementite carbides appear in light contrast.

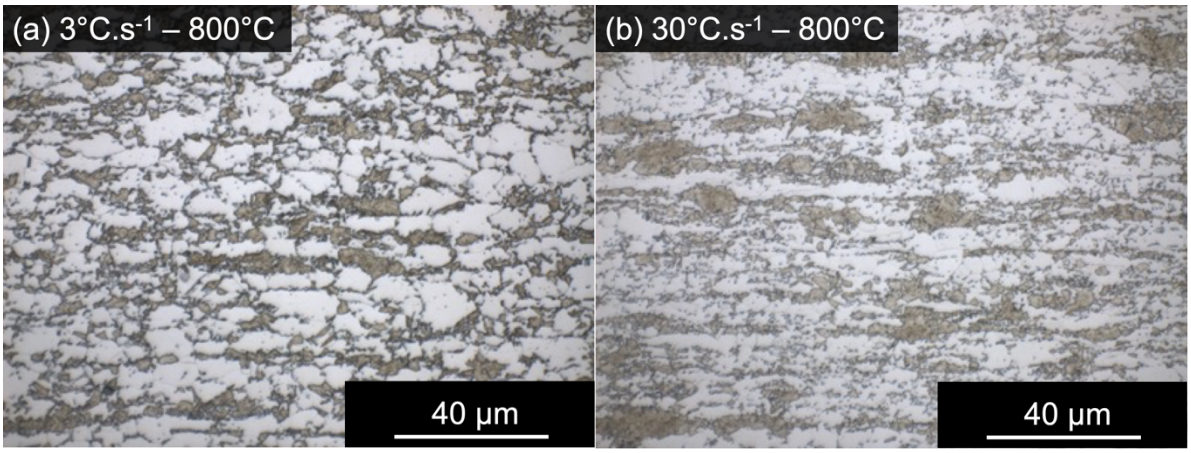

Figure 27. Optical micrographs of the microstructure after heating up to 800°C at a) 3°C.s^{-1}; b) 30°C.s^{-1}.

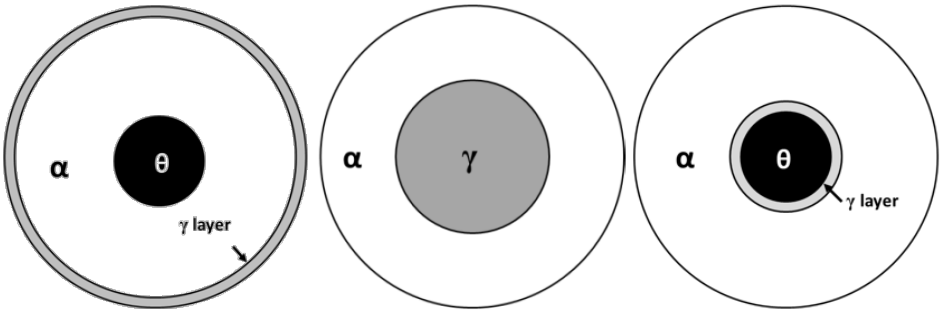

Figure 28. Spherical simulation cells employed in the DICTRA simulations. a) dissolution of a pearlitic cementite carbide (P sub-system); b) Growth of carbon-rich austenite (CRA) grain into ferrite (A sub-system); c) dissolution of an isolated carbide leading to formation of ANC (I sub-system).

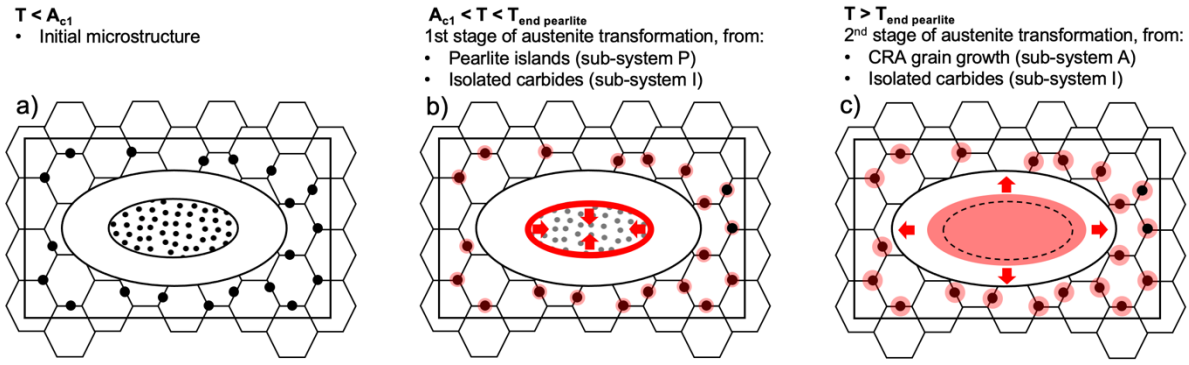

Figure 29. Geometrical representation of the microstructure; two stages of austenite transformation. a) Initial microstructure; b) first stage of austenite transformation; c) second stage.

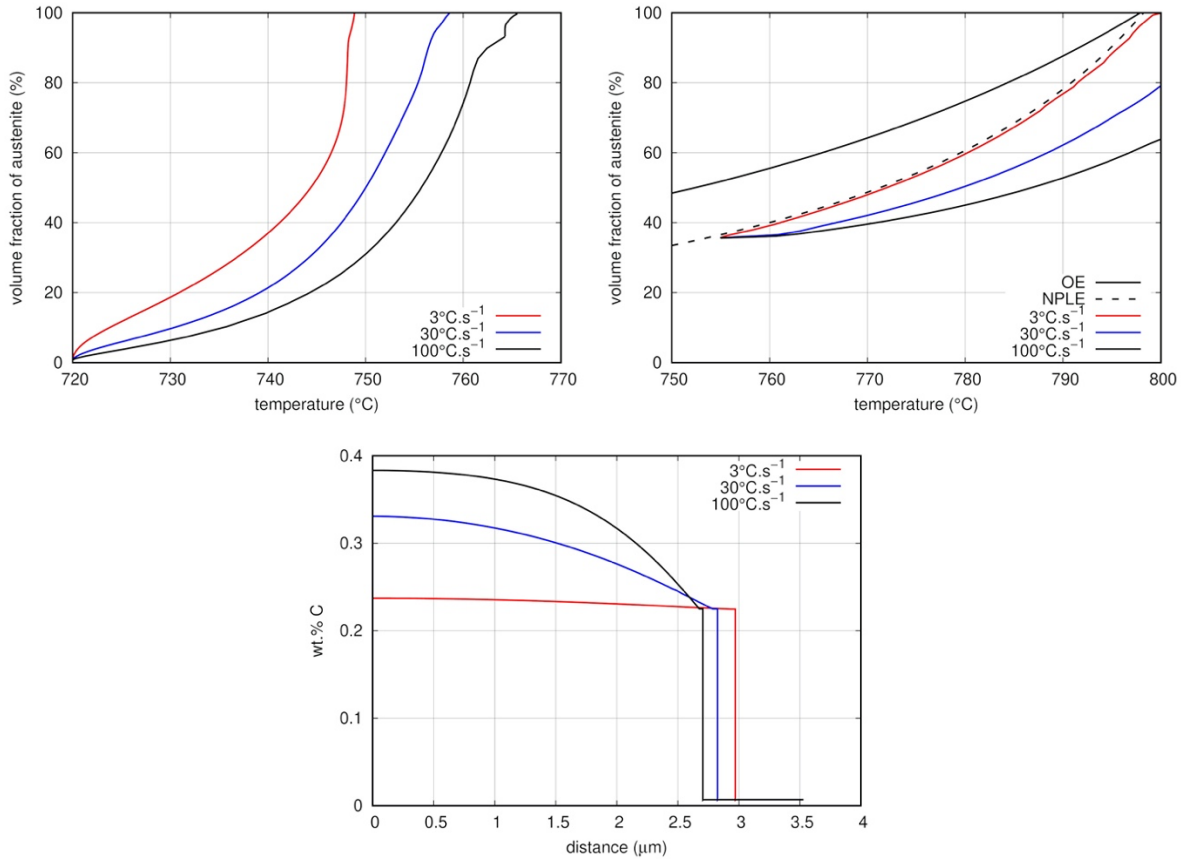

Figure 30. Austenite volume fraction as a function of temperature according to DICTRA simulations inside the simulation cells represented in Figure 12a-b. a) transformation of the pearlite island (sub-system P); b) growth of the CRA grain (sub-system A). OE and NPLE curves represent the austenite volume fraction at equilibrium and after a ferrite to austenite transformation without partition of the Mn; c) carbon concentration profiles at 780°C in simulation cell A, as a function of the distance from the center of the simulation cell.

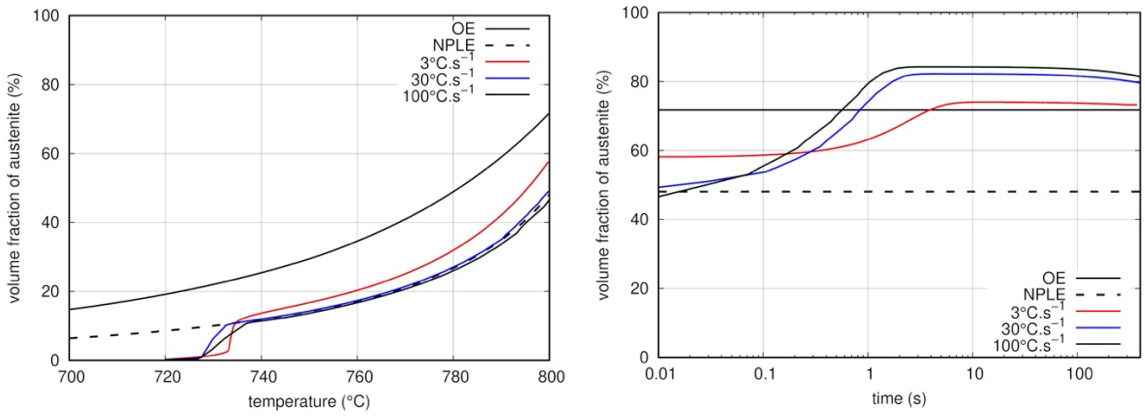

Figure 31. Austenite volume fraction evolution according to DICTRA simulations representative of the isolated carbides dissolution (sub-system I). a) during heating, as a function of temperature; b) during isothermal hold at 800°C. OE and NPLE curves have the same meaning as in Figure 14. (Values are different because of the different overall carbon concentration in cells A and I, see Table 2).

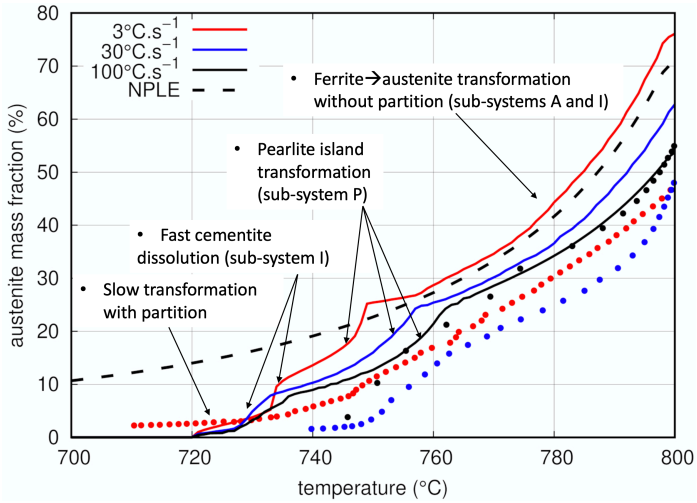

Figure 32. Overall austenite fraction as a function of temperature during heating at 3, 30 and 100°C.s^{-1} according the simulation (lines) and the experiments (dots). Main stages are indicated by the arrows.